Deep Radio Continuum Imaging of Galactic Centre with uGMRT Band 4

M.Sc. Thesis

by

Aditya Prakash Sharma



DEPARTMENT OF ASTRONOMY, ASTROPHYSICS & SPACE ENGINEERING

INDIAN INSTITUTE OF TECHNOLOGY, INDORE

May 2026

Deep Radio Continuum Imaging of Galactic Centre with uGMRT Band 4

A THESIS

Submitted in partial fulfillment of the requirements for the award of the degree
of
Master of Science

by
Aditya Prakash Sharma



DEPARTMENT OF ASTRONOMY, ASTROPHYSICS & SPACE ENGINEERING

INDIAN INSTITUTE OF TECHNOLOGY INDORE

Acknowledgement

I would like to express my sincere gratitude to my supervisor, Dr. Narendranath Patra, for his continuous guidance, support, and encouragement throughout the course of this research work. I am deeply thankful to the faculty members of the Department of Astronomy, Astrophysics & Space Engineering, Indian Institute of Technology Indore, for providing a stimulating academic environment and for their constant support during my M.Sc. programme.

I would also like to acknowledge the use of data from the upgraded Giant Metrewave Radio Telescope (uGMRT), operated by the National Centre for Radio Astrophysics (NCRA-TIFR). I am grateful for the publicly available infrared data from 2MASS and WISE, which enabled the multi-wavelength analysis presented in this thesis.

Finally, I express my heartfelt gratitude to my family for their unwavering support, understanding, and motivation throughout my academic journey. This work would not have been possible without their constant encouragement.

Aditya Prakash Sharma

Dedication

Dedicated to my parents, whose unwavering belief in me has always been my greatest strength; to my brothers, who have stood beside me with constant support; to my sister, whose trust has shaped my confidence and growth as a professional and as a wise person; and to my sister-in-law, whose blessings and encouragement have always guided and protected me.

INDIAN INSTITUTE OF TECHNOLOGY INDORE

CANDIDATE'S DECLARATION

I hereby certify that the work which is being presented in the thesis entitled **Deep Radio Continuum Imaging of the Galactic Centre with uGMRT Band 4** in the partial fulfillment of the requirements for the award of the degree of **MASTER OF SCIENCE** and submitted in the **DEPARTMENT OF Astronomy, Astrophysics and Space Science, Indian Institute of Technology Indore**, is an authentic record of my own work carried out during the time period from July 2024 to May 2026 under the supervision of Dr Narendranath Patra, Assistant Professor, Supervisor.

The matter presented in this thesis has not been submitted by me for the award of any other degree of this or any other institute.

08/05/2026

Signature of the student with date
Aditya Prakash Sharma

This is to certify that the above statement made by the candidate is correct to the best of my/our knowledge.

Narendra Nath Patra.

08.05.2026

Signature of the Supervisor of
M.Sc. thesis (with date)
Dr Narendranath Patra

Aditya Prakash Sharma has successfully given his/her M.Sc. Oral Examination held on **06/05/2026**._____

Narendra Nath Patra.
Signature(s) of Supervisor(s) of MSc thesis
Date: 08.05.2026

Manoneeta Chakraborty
Programme Coordinator, M.Sc.
Date: 08/05/2026

Manoneeta Chakraborty
Convenor, DPGC
Date: 08/05/2026

HoD, DAASE
Date: 08/05/2026

Abstract

We present a radio continuum study of the Galactic Centre region using multi-epoch observations from the upgraded Giant Metrewave Radio Telescope (uGMRT) in Band 4 (550–850 MHz). The primary objectives of this work are to investigate the temporal variability of Sgr A* and to characterize the filamentary structures in the vicinity of the Galactic Centre. The data were processed using standard calibration and imaging techniques, including wide-field imaging and resolution-tapered mapping to recover both compact and diffuse emission. Multi-epoch observations enable a comparative analysis of flux density variations in Sgr A* over time, providing constraints on its variability behaviour at low radio frequencies. Six filamentary structures near the Galactic Centre were identified and analyzed. In-band spectral index mapping reveals flat spectral indices for these filaments, which is inconsistent with the steep negative spectral indices typically associated with synchrotron emission. Furthermore, a comparison with mid-infrared and near-infrared imaging data from WISE and 2MASS shows no corresponding counterparts, suggesting that these structures are unlikely to be of thermal dust origin either. Overall, this study probes the variability of Sgr A* at low radio frequencies and highlights the ambiguous nature of the identified filamentary structures, whose flat spectral indices and lack of MIR/NIR counterparts present an intriguing challenge to standard emission models in the Galactic Centre environment.

TABLE OF CONTENTS

LIST OF FIGURES **5**

1 Introduction **1**
1.1 The Milky Way Galaxy 1
1.2 Structure of the Milky Way 4
1.2.1 Galactic Disk 4
1.2.2 Spiral Arms 5
1.2.3 Galactic Bulge 6
1.2.4 Galactic Halo 6
1.3 The Galactic Plane 7
1.4 The Galactic Center 9
1.5 Interstellar Medium in the Milky Way 11
1.5.1 Molecular Clouds 11
1.5.2 Ionized Gas 12
1.5.3 Dust and Magnetic Fields 12
1.6 Radio Emission in the Galaxy 13
1.6.1 Thermal Free–Free Emission 14
1.6.2 Non–Thermal Synchrotron Emission 14
1.7 Spectral Index 15
1.8 Supernova Remnants 16
1.9 High Energy Phenomena in the Galactic Center 18
1.10 Galactic Plane Radio Surveys 18
1.11 Motivation for the Present Study 20

2 Data Reduction and Processing **23**
2.1 Setting up the Environment 23
2.2 Data Inspection and Flagging 23
2.3 Calibration Workflow 24
2.4 Imaging and Self-Calibration 24
2.5 Pipeline-based processing 25
2.6 Wide-field Imaging with WSClean 26
2.6.1 Why Self-Calibration Was Not Applied 26
2.6.2 Wide-Field Multi-Scale Imaging 26
2.7 Resolution-Tapered Imaging 27
2.8 Contour Analysis and Multi-Wavelength Comparison 27
2.9 Primary Beam Correction 28
2.10 Difference Maps 29
2.11 Percentage Variation Maps 29

3 Results and Discussion **31**
3.1 Full-Field Radio Continuum Maps 31
3.2 Central Region Cutout Maps 32

3.3 Resolution-Tapered Images . . . 33
3.3.1 Full-Field Tapered Images . . . 34
3.3.2 Cutout Tapered Images . . . 35
3.4 Primary Beam Corrected Images and Light Curve of the Central Source 37
3.5 Difference Maps . . . 41
3.6 Percentage Variation Maps . . . 46
3.7 In-Band Spectral Index Maps of Some of the filaments near GC . . . 52
3.7.1 G359.78+0.17 . . . 52
3.7.2 G359.55+0.18 . . . 53
3.7.3 G359.83-0.28 . . . 54
3.7.4 G359.83-0.28 . . . 55
3.7.5 Radio Arc . . . 56
3.7.6 G359.45-0.04 . . . 57
3.8 Physical Lengths of Identified Filaments . . . 58
3.9 Multi-wavelength Comparison with Infrared Data . . . 59
3.10 Summary . . . 60

4 Future Plans **63**
4.1 Characterisation of the Detected Filaments . . . 63
4.2 Identifying New SNR Candidates . . . 63
4.3 Multi-frequency Follow-up . . . 63

LIST OF FIGURES

1.1 The Milky Way Galaxy 2

1.2 Spitzer 360 image of our Milky Way 3

1.3 Structure representation of our Milky Way 4

1.4 Galactic disk of the Milky Way 5

1.5 Spiral Arms of the Milky way 5

1.6 Galactic Bulge of the Milky Way 6

1.7 Galactic Halo of the Milky Way 7

1.8 Galactic Plane of the Milky Way 8

1.9 Galactic Center of the Milky Way 10

3.1 Full-field uGMRT Band 4 (550–850 MHz) radio continuum images of the Galactic Centre region across five observing epochs (3.13.1.1–3.13.1.5). The dominant central source is the Sgr A complex (Balick and Brown, 1974), visible as a bright compact structure near pixel coordinates $(3000, 3000)$ in each epoch. Faint diffuse emission and extended radio structures are visible in the surrounding field. 31

3.2 WCS-cutout images of the central Galactic Centre region extracted from the full-field uGMRT Band 4 maps for each of the five observing epochs. The field spans approximately $17^{h}44^{m}$ to $17^{h}48^{m}$ in right ascension and $-2830'$ to $-2930'$ in declination. The colour scale represents intensity in Jy beam^{-1}. The bright central source is the Sgr A complex, surrounded by a rich network of diffuse emission and non-thermal filamentary structures. 32

3.3.1 Full-field resolution-tapered (20-arcsecond uv-taper) images of the Galactic Centre region for all five observing epochs. The Sgr A complex is visible as the bright compact structure near pixel coordinates (3000, 3000) in each epoch. The colour scale represents intensity in Jy beam^{-1}. . . . 35

3.3.2 Resolution-tapered (20-arcsecond uv-taper) cutout images of the central Galactic Centre region for all five observing epochs. The field is centred on the Sgr A complex. The colour scale represents intensity in Jy beam^{-1}. Extended diffuse emission and filamentary structures to the north of the central source are prominently recovered compared to the full-resolution cutout maps. 36

3.3.2 Light curve of the integrated flux density measured at the fixed pixel position (x = 3001, y = 3001) using a compact aperture centred on the location of Sgr A*, constructed from the primary beam corrected uGMRT Band 4 images across the five observing epochs. The x-axis shows the observation date extracted from the FITS headers (DATE-OBS) and the y-axis shows the integrated flux density in mJy. Error bars represent $\pm\,\sigma_{\rm rms}$ of each epoch image. The flux densities lie in the range ∼534–775 mJy, with an apparent peak during the 14 January epoch (Roy and Pramesh Rao, 2004). However, as discussed in the text, at Band 4 frequencies Sgr A* is heavily scatter-broadened by the intervening ionised medium (Bower et al., 2006) and cannot be cleanly isolated from the surrounding extended emission. The epoch-to-epoch variation visible here is therefore attributed primarily to imaging systematics — including beam size differences, uv-coverage variations, and residual calibration offsets between epochs — rather than to genuine intrinsic variability of Sgr A* itself. 38
3.3.2 Light curve of the integrated flux density of the central Galactic Centre region (Sagittarius A complex), measured from the primary beam corrected uGMRT Band 4 images across the five observing epochs. The aperture is centred at pixel position (x = 3001, y = 3001) and encompasses the Sgr A complex together with the surrounding extended emission. The x-axis shows the observation date extracted from the FITS headers (DATE-OBS) and the y-axis shows the integrated flux density in Jy. The flux densities lie in the range ∼303–352 Jy, consistent with the known total radio flux of the Galactic Centre complex at Band 4 frequencies. A local minimum is visible during the 22 February epoch, while the 01 April epoch shows the highest recovered flux. . . . 39
3.3.2 Difference map for the epoch pair 26 Oct − 14 Nov. The colour scale is symmetric logarithmic spanning $\pm10^{-2}$ to $\pm10^{-1}$ Jy beam^{-1}. Positive residuals (26 Oct brighter) are shown in yellow-green and negative residuals (14 Nov brighter) in blue-purple. 41
3.3.2 Difference map for the epoch pair 26 Oct − 14 Jan. Colour scale as in Figure 3.3.2. 42
3.3.2 Difference map for the epoch pair 26 Oct − 22 Feb. Colour scale as in Figure 3.3.2. 42
3.3.2 Difference map for the epoch pair 26 Oct − 01 Apr. Colour scale as in Figure 3.3.2. 43
3.3.2 Difference map for the epoch pair 14 Nov − 14 Jan. Colour scale as in Figure 3.3.2. 43
3.3.2 Difference map for the epoch pair 14 Nov − 22 Feb. Colour scale as in Figure 3.3.2. 44
3.3.2 Difference map for the epoch pair 14 Nov − 01 Apr. Colour scale as in Figure 3.3.2. 44
3.3.2 Difference map for the epoch pair 14 Jan − 22 Feb. Colour scale as in Figure 3.3.2. 45
3.3.2 Difference map for the epoch pair 14 Jan − 01 Apr. Colour scale as in Figure 3.3.2. 45

3.3.2 Difference map for the epoch pair 22 Feb − 01 Apr. Colour scale as in Figure 3.3.2. 46
3.3.2 Percentage flux variation map for the epoch pair 26 Oct/14 Nov. The colour scale runs linearly from 0% (dark purple, low fractional variation) to 7% (yellow, high fractional variation). 47
3.3.2 Percentage flux variation map for the epoch pair 26 Oct/14 Jan. Colour scale as in Figure 3.3.2. 48
3.3.2 Percentage flux variation map for the epoch pair 26 Oct/22 Feb. Colour scale as in Figure 3.3.2. 48
3.3.2 Percentage flux variation map for the epoch pair 26 Oct/01 Apr. Colour scale as in Figure 3.3.2. 49
3.3.2 Percentage flux variation map for the epoch pair 14 Nov/14 Jan. Colour scale as in Figure 3.3.2. 49
3.3.2 Percentage flux variation map for the epoch pair 14 Nov/22 Feb. Colour scale as in Figure 3.3.2. 50
3.3.2 Percentage flux variation map for the epoch pair 14 Nov/01 Apr. Colour scale as in Figure 3.3.2. 50
3.3.2 Percentage flux variation map for the epoch pair 14 Jan/22 Feb. Colour scale as in Figure 3.3.2. 51
3.3.2 Percentage flux variation map for the epoch pair 14 Jan/01 Apr. Colour scale as in Figure 3.3.2. 51
3.3.2 Percentage flux variation map for the epoch pair 22 Feb/01 Apr. Colour scale as in Figure 3.3.2. 52
3.4.1 In-band spectral index maps of G359.78+0.17 for all four observing epochs. The colour scale represents the spectral index α, where $S_\nu \propto \nu^\alpha$. 53
3.4.2 In-band spectral index maps of G359.55+0.18 for all five observing epochs. The colour scale represents the spectral index α, where $S_\nu \propto \nu^\alpha$. 54
3.4.3 In-band spectral index maps of G359.83−0.28 for all five observing epochs. The colour scale represents the spectral index α, where $S_\nu \propto \nu^\alpha$. 55
3.4.4 In-band spectral index maps of G0.08+0.15 for all five observing epochs. The colour scale represents the spectral index α, where $S_\nu \propto \nu^\alpha$. 56
3.4.5 In-band spectral index maps of the Radio Arc for all five observing epochs. The colour scale represents the spectral index α, where $S_\nu \propto \nu^\alpha$. 57
3.4.6 In-band spectral index maps of G359.45−0.04 for all five observing epochs. The colour scale represents the spectral index α, where $S_\nu \propto \nu^\alpha$. 58
3.6 Multi-epoch overlay of uGMRT Band 4 radio continuum emission with infrared contours (WISE) for the Galactic Centre region. The colour scale represents radio flux density (mJy beam^{-1}), while green contours indicate infrared emission. The central bright source corresponds to the Sgr A complex. Extended diffuse emission and filamentary structures are visible, with partial correspondence to infrared features, indicating a mixture of thermal and non-thermal emission processes. 60
3.7 Multi-epoch overlay of uGMRT Band 4 radio continuum emission with 2MASS infrared contours for the Galactic Centre region. The infrared emission traces stellar populations and dust, while the radio emission reveals both compact and diffuse structures. The comparison highlights differences between thermal infrared emission and non-thermal radio emission, particularly in the filamentary regions. 60

Chapter 1

Introduction

1.1 The Milky Way Galaxy

The Milky way galaxy that contains our Solar System. It is a barred spiral galaxy that consists of stars, stellar remnants, gas, dust, magnetic fields, and a dominant component of Dark matter and our solar system resides within the Galactic disk so our view of the Milky Way is different from other external galaxies, and also our understanding of its structure has been derived through indirect observational methods (Hou, Han, and Shi, 2009). When the Milky way observed from Earth under dark sky, the Milky way appears as a faint, diffuse band of light extending across the celestial sphere. This radiant band arises from the integrated emission of billions of unresolved stars located along the galactic plane. As some stars are visible to naked eyes, but majority of stars in the Galaxy are too distant to be resolved individually without telescopes.
The Milky way is classified as a barred spiral galaxy of type SBbc in the Hubble morphological classification scheme. Which means that, observational evidence, it contains central bar structure surrounded by several loosly wound spiral arms that extent outward through the Galactic disk. (Shen and Zheng, 2020). The disk itself is embedded within a much larger halo of dark matter that dominates the Galaxy's gravitational potential. Now the size of the Milky Way has been estimated through a variety of observational techniques including star counts, measurements of stellar motions, and radio observations of neutral hydrogen. Current estimates suggest that the stellar disk of the Galaxy has a diameter of around 26 Kpc (about 85,000 ly). However, the dark matter halo extends far beyond the visible disk. The total mass of the Milky Way remains uncertain but is generally estimated to lie within the range

$$M_{\mathrm{MW}} \approx (0.8 - 1.3) \times 10^{12} M_{\odot}$$

where $M_{\odot}$ represents the solar mass. Only a small fraction of this mass is contained in visible stars and gas, while the majority is believed to consist of dark matter. The presence of dark matter is inferred primarily from the observed rotation curve of the Galaxy (Navarro, Frenk, and White, 1996).

In a gravitationally bound system, the circular velocity of an object orbiting at radius r from the center is given by

$$v(r) = \sqrt{\frac{GM(r)}{r}}$$

where G is the gravitational constant and $M(r)$ is the total mass enclosed within radius r. If mass distribution of the galaxy were dominated only by visible matter concentrated near the centre, the orbital velocity would decrease with increasing radius. However, observations show that the rotation curve of the Milky way remains almost flat at large distances from the Galactic centre, Which shows that additional unseen mass must be present in the form of an extended dark matter halo.

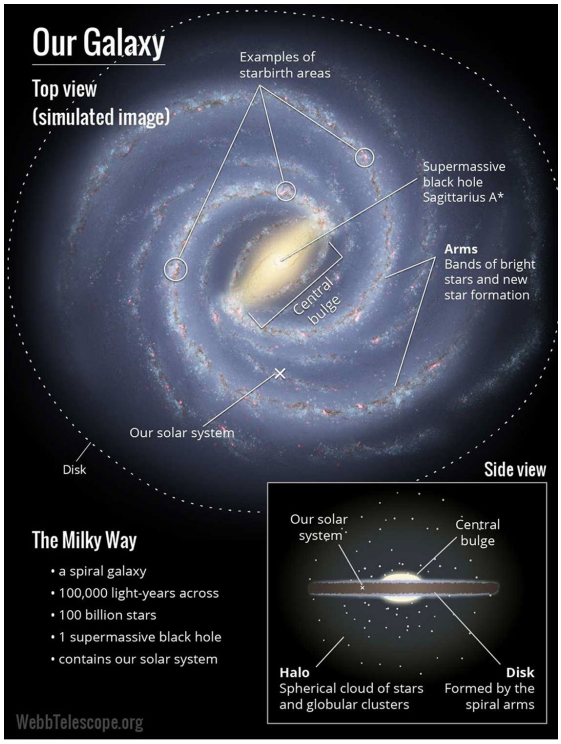

Figure 1.1: The Milky Way Galaxy

The Solar System is located within the Galactic disk at a distance of approximately 8.2 kpc from the Galactic Centre (Ciurlo and M. R. Morris, 2025). This location places the Sun within a minor spiral feature known as the Orion–Cygnus arm or Orion spur. The Sun lies roughly 20 pc above the mid-plane of the Galactic disk and orbits the Galactic Center with a velocity of approximately 220 km s^{-1}.

The orbital period of the Sun around the Galaxy can be estimated using the relation

$$T = \frac{2\pi R}{v}$$

where R is the galacto-centric distance and v is the orbital velocity. Substituting the appropriate values yields an orbital period of roughly 2.3×10^8 years. This period is often referred to as a "Galactic year". Since the formation of the Solar System approximately 4.6 billion years ago, the Sun has completed roughly twenty such orbits around the Galactic Center.

The stellar population of the Milky Way is extremely diverse spanning a wide range of masses, ages, and chemical compositions. Young massive stars are typically found in the spiral arms where active star formation is taking place, while older stellar populations are distributed throughout the Galactic disk and halo. Stellar evolution processes continuously recycle material into the interstellar medium through stellar winds, planetary nebulae, and supernova explosions. Also, the galaxy contains a significant amount of interstellar gas and dust and this material forms the ISM, which plays a fundamental role in the formation of new stars. The interstellar medium contains mainly hydrogen and helium as well as trace amounts of heavier elements. It also has multiple phases like cold molecular gas, warm neutral gas, warm ionized gas, and hot ionised plasma. Another important component of the Milky way is population of stellar remnants and compact objects, which includes White dwarfs, neutron stars, and stellar-mass black

holes formed through the evolution of massive stars. Numerous star clusters that provide important insights into stellar evolution and Galactic dynamics exist in the Milky way. Here, Open clusters are generally found within the Galactic disk and contain relatively young stars that formed from the same molecular cloud, and Globular clusters are much older and distributed in the Galactic halo. These clusters often contain hundreds of thousands of stars and are among the oldest known objects in the Galaxy. As the entire electromagnetic spectrum used for observational studies of the Milky way. In which, Optical observations provide information about the stellar populations, while infrared observations allow to probe regions covered by interstellar dust. While the radio observations are important for studying the distribution of gas and the presence of non-thermal emission from objects such as supernova remnants and pulsars. In recent time, large-scale astronomical surveys have greatly improved our understanding of the Milky way.
Infrared surveys such as the Two Micron All Sky Survey (2MASS) and Spitzer Galactic surveys have revealed the detailed structure of the Galactic bulge and bar and also radio surveys of neutral hydrogen (H I) and molecular gas have mapped the spiral structure of the galaxy (Hou, Han, and Shi, 2009).
Recently, We get to know the precise measurements of stellar positions and motions by Gaia, which help us to construst the 3D maps of the Milky way.

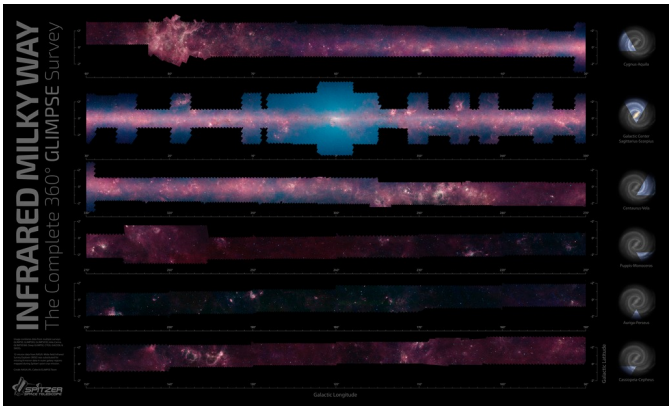

Figure 1.2: Spitzer 360 image of our Milky Way

But after all this, there are many aspects of the Milky Way that remain to be understood. But due to the position of our solar system in the galactic disk, makes it difficult to get the global view of the galaxy's structure. Observation of the inner galaxy are complicated by strong extinction from interstellar dust and by the large number of overlapping sources along the line of sight. As a result, radio observation play a crucial role in studying the galactic plane and the energetic phenomera that occur within it. And Structure and evolution of the Milky way understanding is essential not only for galactic astronomy but also for the broader study of the galaxy formation and evolution, and we can only observe the Milky way in great details, the Milky way serves as a fundamental laboratory for testing theories of stellar evolution, interstellar medium dynamics, and the formation of large-scale cosmic structures.

1.2 Structure of the Milky Way

The Milky way is a complex astrophysical system consists of different components which have different stellar populations, kinematics, and spatial distributions.
By observations, it can interpret that galaxy can be broadly divided into four principal components: the Galactic disk, the spiral arms, the central bulge, and the extended halo, and every component plays an important role in the overall evolution and dynamics of the Galaxy (Shen and Zheng, 2020). Because the Solar system is within the Galactic disk, so determining the large-scale structure of the Milky way is considerably more challenging than studying external galaxies. So we have to use indirect methods such as star counts, measurements of stellar motions, observations of interstellar gas, and mapping of radio emission from neutral hydrogen and molecular clouds. Over the past several decades. Because the Solar System is located within the Galactic disk, determining the large-scale structure of the Milky Way is considerably more challenging than studying external galaxies. We therefore rely on indirect methods such as star counts, measurements of stellar motions, observations of interstellar gas, and mapping of radio emission from neutral hydrogen and molecular clouds (Hou, Han, and Shi, 2009). Over the past several decades, observations across multiple wavelengths have provided increasingly detailed insights into the structure of our Galaxy.

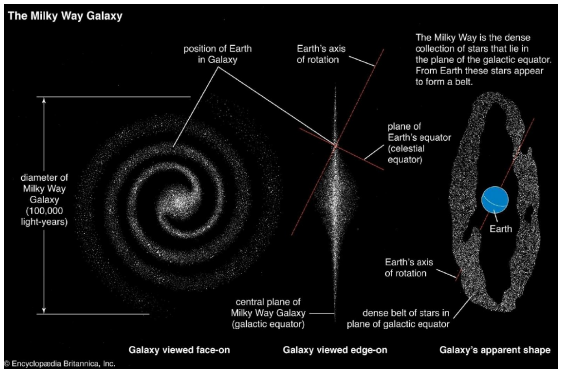

Figure 1.3: Structure representation of our Milky Way

1.2.1 Galactic Disk

The Galactic disk represents the dominant visible component of the Milky Way and contains the majority of the Galaxy's stars, gas, and dust. The disk is a flattened rotating structure with a radius of approximately 13 kpc and a vertical thickness of a few hundred parsecs. The stellar density within the disk decreases exponentially with increasing distance from the Galactic center. The radial distribution of stars in the disk is often described by an exponential surface density profile of the form

$$\Sigma(R) = \Sigma_0 e^{-R/R_d}$$

where $\Sigma(R)$ represents the surface density at radius R, Σ_0 is the central surface density, and R_d is the disk scale length. Observations indicate that the scale length of the Milky Way disk is approximately 2.5 - 3.5 kpc (Shen and Zheng, 2020). Also, the stellar density decreases approximately exponentially with height above the Galactic plane. This distribution can be expressed as

$$\rho(z) = \rho_0 e^{-|z|/h_z}$$

where h_z is the vertical scale height of the disk. The thin disk component of the Galaxy has a scale height of roughly 300 pc, while the thick disk has a larger scale height of approximately 1 kpc. The thick disk contains older and more metal-poor stars compared to the thin disk.

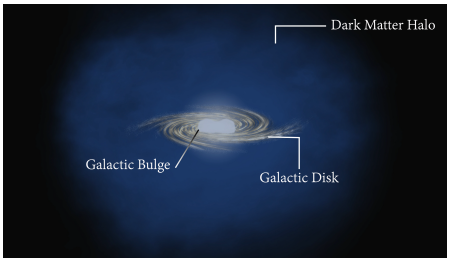

Figure 1.4: Galactic disk of the Milky Way

Star formation occurs primarily within the Galactic disk, particularly in regions where the density of molecular gas is high. These regions are often associated with spiral arms and giant molecular clouds, which serve as the birthplaces of new stars.

1.2.2 Spiral Arms

The Milky way consists of several arms that extend outward from the central bar. Spiral arms has high density zones where gas, dust, and young stars are concentrated. These structures are often traced by observations of H II regions, molecular clouds, and massive young stars (Hou, Han, and Shi, 2009). Empirical evidence suggests that the Milky way contains four primary spiral arms:

- Perseus Arm
- Scutum-Centaurus Arm
- Sagittarius-Carina Arm
- Norma Arm

While Milky way has some of the smaller spiral arms:

- Orion–Cygnus Spur
- Orion Spur

In addition to these major and smaller arms, the Solar System is located within a smaller feature known as the Orion–Cygnus spur.



Figure 1.5: Spiral Arms of the Milky way

The angular velocity of stars in the Galaxy is given by

$$\Omega(R) = \frac{v(R)}{R}$$

where $v(R)$ is the circular velocity at radius R. The spiral pattern itself rotates with a different angular speed known as the pattern speed, which is typically lower than the orbital velocities of stars.

1.2.3 Galactic Bulge

Galactic bulge, which lies at the center of the Milky way, a dense spheroidal concentration of stars extend roughly 2kpc from the Galactic Center.
The galactic bulge contains predominantly old stars with relatively high metallicities, indicating that it formed early in the Galaxy's history.

Infrared observations have revealed that the bulge has a boxy or peanut-shaped morphology rather than a simple spherical structure (Shen and Zheng, 2020). This shape is thought to result from dynamical instabilities in the Galactic bar, which cause stars to move above and below the Galactic plane.



Figure 1.6: Galactic Bulge of the Milky Way

The stellar density in the bulge is significantly higher than in the disk, and the velocity dispersion of stars in this region is correspondingly higher. The bulge also contains numerous compact objects, including neutron stars and stellar-mass black holes, as well as the supermassive black hole Sagittarius A* located at the dynamical center of the Galaxy (Ciurlo and M. R. Morris, 2025).

1.2.4 Galactic Halo

The Galactic halo, surrounding the Galactic disk and the bulge, is an extended halo consisting of old stars, globular clusters, and dark matter. Observations showed that stellar halo contains some of the most metal-poor stars in the galaxy, which means that these stars formed during the early stages of the galactic evolution.
The halo extendes more than 100 kpc from the Galactic Center and has a roughly spherical distribution.
The stellar density in the halo decreases approximately as a power law with increasing radius by:

$$\rho(r) \propto r^{-n}$$

where the exponent n is typically between 2.5 and 3.5.

In addition to stars, the halo contains a large population of globular clusters. These clusters are among the oldest stellar systems known and provide valuable information about the early formation history of the Milky Way.



Figure 1.7: Galactic Halo of the Milky Way

Dark matter, the most massive component of the halo, dominated the gravitational potential of the Galaxy. Although dark matter can't be observed directly but its presence is inferred from the dynamics of stars and gas within the Galaxy. One commonly used model for the density distribution of dark matter halos is the Navarro–Frenk–White (NFW) profile (Navarro, Frenk, and White, 1996), given by

$$\rho(r) = \frac{\rho_0}{(r/r_s)(1 + r/r_s)^2}$$

where ρ_0 is a characteristic density and r_s is a scale radius. This profile arises naturally in numerical simulations of structure formation in the universe.

The dark matter halo plays a crucial role in maintaining the stability of the Galactic disk and explaining the observed flat rotation curve of the Milky Way (Navarro, Frenk, and White, 1996).

1.3 The Galactic Plane

The Galactic plane is defined as the mid-plane of the Milky way's disk, where the majority of the Galaxy's stellar mass, interstellar gas, and dust are concentrated. In disk galaxies such as the Milky way, stars and gas orbit within a relatively thin, rotating disk structure, and the plane defind by this disk is referred to as the Galactic Plane because the solar system itself lies within this disk, our observational perspective of the Galaxy is strongly influenced by structures located along this plane. Most of the prominent astrophysical processes occurring in the Milky way take place within or near the Galactic Plane. These include star formation, evolution of massive stars, supernova explosions, and the formation of complex structures in the interstellar medium. The position of the Galactic plane is defined within the Galactic coordinate system, which is commonly used in the studies of Galactic structure. In this coordinate system, the Galactic plane corresponds to Galactic latitude $b = 0°$. The north Galactic pole lies in the constellation Coma Berenices, while the Galactic Center is located at Galactic

longitude $l = 0°$ in the direction of Sagittarius. Galactic coordinates allows us to map the distribution of objects within the Galaxy relative to the plane of the disk.

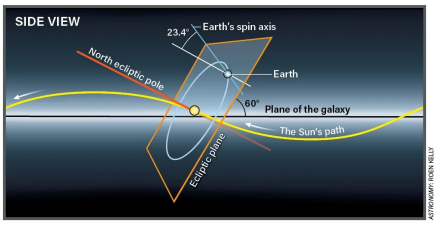

Figure 1.8: Galactic Plane of the Milky Way

The structure of the Galactic Plane is not uniform. Instead, it contains a wide range of structures including spiral arms, molecular clouds, star-forming regions, supernova remnants, and compact objects such as neutron stars and black holes. The density of interstellar gas and dust is particularly high within the plane, which plays a crucial role in the formation of new stars. One of the defining characteristics of the Galactic Plane is the presence of spiral arms. These spiral arms represent regions of enhanced density within the disk and contain large concentrations of molecular gas and young stars (Hou, Han, and Shi, 2009). Giant molecular clouds within these arms serve as the primary sites of star formation. When gravitational instabilities cause these clouds to collapse, new stars are formed, often in clusters.
The distribution of gas in the Galactic plane can be studied using radio observations of neutral hydrogen (HI) at the wavelength of 21 cm. The 21 cm emission line arises from the hyperfine transition of neutral hydrogen atoms and provides a powerful tool for mapping the distribution and kinematics of gas throughout the galaxy. Observations of this line have revealed the large-scale spiral structure of the Milky way and have been used to determine the rotation curve of the Galaxy (Hou, Han, and Shi, 2009). In addition to neutral hydrogen, molecular gas is also abundant in the Galactic Plane. Molecular hydrogen (H_2) is the most common molecule in the interstellar medium, although it is difficult to observe directly. Instead, We often use carbon monoxide (CO) as a tracer of molecular gas. Observations of CO emission lines have been used to map the distribution of molecular clouds in the Galactic disk. The density of molecular gas within the Galactic plane is linked to star formation activity. Regions with high concentrations of molecular gas often host large numbers of young stars and H II regions. H II regions are formed when UV radiation from hot, massive stars ionizes the surrounding gas. These regions emit strongly at radio wavelengths due to free-free emission from ionized plasma. Although the Galactic plane is rich in astrophysical phenomena, observations of this region at optical wavelengths are significantly hindered by interstellar dust. Dust particle absorb and scatter visible light, producing a phenomenon known as interstellar extinction. As a result, distant objects within the Galactic plane are often obscured in optical observations. The effect of extinction can be quantified by the relation

$$I = I_0 e^{-\tau}$$

where I_0 is the intrinsic intensity of the radiation, I is the observed intensity, and τ represents the optical depth of the intervening material. Large values of τ correspond to strong attenuation of the radiation. And because radio waves are much less affected by interstellar dust than optical radiation, radio observations are enough good for studying

the Galactic plane. Radio telescopes can detect emission from gas, dust, and non-thermal processes that are otherwise hidden at shorter wavelengths. Also one of the most important advantages of radio observations is their ability to detect synchrotron emission produced by relativistic electrons moving in magnetic fields. Such emission is commonly associated with supernova remnants, pulsar wind nebulae, and other high-energy astrophysical phenomena. Another important feature of the Galactic plane is the presence of large-scale magnetic fields. These magnetic fields play a significant role in shaping the dynamics of the interstellar medium. The strength of the magnetic field in the Galactic disk is typically of the order of a few microgauss, although stronger fields can exist in localized regions such as the Galatic Center. Magnetic fields can be studies through observations of polarized radio emission. When synchrotron radiation is emitted by relativistic electrons spiraling around magnetic field lines, this resulting radiation is partially polarized. Measurements of this polarization provide important information about the orientation and strength of magnetic fields in the Galaxy. Also the high density of sources and the presence of complex diffuse emission, the Galactic plane presents unique observational challenges. High angular resolution and high sensitivity are required in order to distinguish individual sources from the surrounding background emission. Furthermore, radio surveys of the Galactic plane play a crucial role in identifying previously unknown SNRs and other non-thermal sources. Many of these objects are faint and extended, making them difficult to detect in surveys with limited sensitivity.

1.4 The Galactic Center

The Galactic Center (GC) represents the dynamical and gravitational core of the Milky Way galaxy and lies in the direction of the constellation Sagittarius. It is located at a distance of approximately $\sim$ 8.2 kpc (about 27 000 light–years) from the Solar System (Ciurlo and M. R. Morris, 2025). The Galactic Center region is one of the most complex and energetic environments in the Galaxy, containing dense molecular gas, intense radiation fields, strong magnetic fields, and a high concentration of massive stars. Because of the large amount of interstellar dust along the Galactic plane, optical observations of this region are heavily obscured. As a result, most studies of the Galactic Center are conducted using infrared, radio, X-ray, and gamma-ray observations.

The central region of the Galaxy is characterized by an unusually high density of stars. The stellar density in the innermost parsec is several orders of magnitude greater than that found in the Solar neighborhood. This region contains a mixture of stellar populations including old evolved stars as well as young massive stars. The presence of these young stars suggests that star formation can occur even in the extreme environment near the Galactic Center.

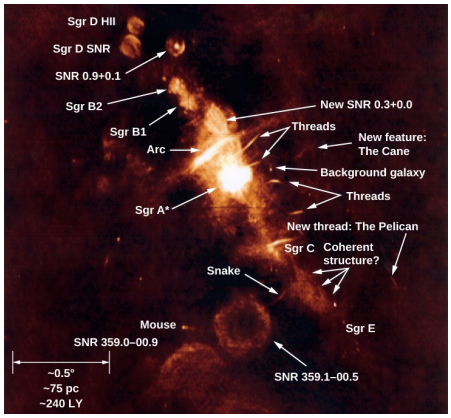

Figure 1.9: Galactic Center of the Milky Way

At the very center of the Milky way lies a compact radio source known as Sagittarius A* (Sgr A*), which is widely accepted as the location of the Galaxy's central supermassive black hole. Observations of stellar motions around this object have provided some of the most important evidence for the existence of supermassive black haloes in galactic nuclei (Ciurlo and M. R. Morris, 2025).
High resolution infrared observations have revealed a group of stars orbiting extremely close to Sgr A*. The orbital parameters of these stars indicate that they are bound to a compact object with a mass of approximately-

$$M_{\mathrm{BH}} \approx 4.1 \times 10^{6} M_{\odot}.$$

One study, known as S2, follows an elliptical orbit with a period of about 16 years and approaches the central black hole to within a distance of roughly 120 AU. The motion of such stars can be described by Keplerian dynamics, where the orbital velocity v of the star is-

$$v = \sqrt{\frac{GM}{r}}.$$

Surrounding the immediate region of Sgr A* is a region known as the Central Molecular Zone (CMZ), which extends roughly 500 pc from the Galactic Center. The CMZ contains a large concentration of molecular gas and represents one of the most active star-forming regions in the Galaxy. Molecular clouds in this region have masses ranging from 10^4 to 10^7 solar masses and exhibit unusually high temperatures and turbulent velocities compared to typical molecular clouds in the Galactic disk.

The energy density of the interstellar medium in the Galactic Center is significantly higher than that in the Solar neighborhood. The density of molecular gas, cosmic rays, and magnetic fields in this region can exceed typical disk values by one to two orders of magnitude. These extreme physical conditions influence the dynamics of the interstellar medium and affect the processes of star formation and particle acceleration. Some prominent young stellar clusters are located in the Galactic Center region, among the most notable are the Arches Cluster and the Quintuplet Cluster. These clusters contain large populations of massive stars, including O-type and Wolf-Rayet stars. The intense stellar winds and radiation from these stars inject large amounts of energy into the surrounding interstellar medium, contributing to the complex dynamics observed in the central region (Ciurlo and M. R. Morris, 2025).
Also the Galactic center hosts numerous non-thermal filaments (NTFs), which emi

synchrotron radiation from relativistic electrons and are likely associated with large-scale magnetic field oriented perpendicular to the Galactic plane. The magnetic field strength in this region is significantly higher than in the Galactic disk, reaching values of several hundred microgauss.
In addition to radio emission, the Galactic Center is a strong source of high-energy radiation. X-ray observations reveal compact objects such as neutron stars and black hole candidates, along with diffuse hot plasma, while gamma-ray studies have identified large-scale structures like the Fermi bubbles extending up to aroung 25,000 light-years.

1.5 Interstellar Medium in the Milky Way

The space between stars is not empty but is filled with a mixture of gas, dust, cosmic rays, and magnetic fields, collectively known as the interstellar medium (ISM). The ISM plays a fundamental role in the life cycle of stars and in the dynamical evolution of galaxies. Material ejected from stars through stellar winds, planetary nebulae, and supernova explosions enriches the interstellar medium with heavy elements. In result, dense regions within the ISM collapse under gravity to form new generations of stars. The interstellar medium in the Milky way is composed primarily of hydrogen and helium, with hydrogen accounting for nearly 90% of the atomic content by number. The remaining fraction consists of heavier elements and interstellar dust particles. Despite its low density compared to terrestrial environments, the ISM contains a significant amount of mass when integrated over the entire volume of the Galaxy. Estimates suggest that roughly 10-15% of the visible baryonic mass of the Milky way is contained within the interstellar medium. ISM contains Molecular clouds, Ionized gas, Dust, and Magnetic field and these are as following:

1.5.1 Molecular Clouds

Molecular clouds represent the coldest and densest component of the interstellar medium and serve as the primary sites of star formation in the Galaxy. These clouds consist mainly of molecular hydrogen (H_2), although the molecule itself is difficult to observe directly because it lacks a permanent dipole moment. Instead, We commonly use carbon monoxide (CO) emission lines as tracers of molecular gas.

Typical temperatures within molecular clouds are on the order of 10-20 K, while particle densities can range from 10^2 to 10^6 cm^{-3}. Giant molecular clouds may contain masses exceeding 10^5 solar masses and extend over tens of parsecs. The gravitational stability of these clouds is often described by the Jeans criterion. A cloud will collapse gravitationally when its mass exceeds the Jeans mass given by

$$M_J \approx \left(\frac{5kT}{G\mu m_H}\right)^{3/2} \rho^{-1/2},$$

where T is the temperature of the gas, ρ is the mass density, μ is the mean molecular weight, m_H is the mass of a hydrogen atom, k is Boltzmann's constant, and G is the gravitational constant.
When gravitational collapse occurs, dense cores form within molecular clouds, eventually giving rise to proto-stars.

Molecular clouds are highly structured and turbulent. Supersonic turbulence within these clouds produces a hierarchy of density fluctuations, which influences the formation

of stars and stellar clusters. Magnetic fields also play a role in regulating the collapse of molecular gas by providing additional pressure support against gravity.

1.5.2 Ionized Gas

Ionized gas is another important component of the interstellar medium and is commonly found in regions surrounding young massive stars. These regions, known as H II regions, are formed when ultraviolet radiation from hot O- and B-type stars ionizes the surrounding hydrogen gas. The resulting plasma emits strongly at optical and radio wavelengths.

The temperature of ionized gas in H II regions typically lies near 10^4 K, while the electron density may range from a few particles per cubic centimeter to several thousand in dense regions. Radio observations of H II regions provide valuable information about star formation activity in the Galaxy because free–free emission from ionized gas can be detected even in regions heavily obscured by dust.

1.5.3 Dust and Magnetic Fields

Interstellar dust constitutes roughly 1% of the mass of the interstellar medium but has a significant impact on astronomical observations. Dust grains are composed of silicates, carbonaceous materials, and other heavy elements. These grains absorb and scatter optical and ultraviolet radiation, producing the phenomenon known as interstellar extinction.

The effect of dust extinction can be described by the relation

$$I = I_0 e^{-\tau},$$

where I_0 is the intrinsic intensity of radiation emitted by a source, I is the observed intensity, and τ is the optical depth along the line of sight. In regions with large optical depths, optical radiation is strongly attenuated, making observations difficult.

While dust obscures optical radiation, it also re-emits absorbed energy at infrared wavelengths. Infrared observations have therefore become an essential tool for studying star-forming regions embedded within dense molecular clouds.

Magnetic fields are another important component of the interstellar medium. Observations indicate that the typical strength of the Galactic magnetic field in the disk is on the order of a few microgauss. Although relatively weak compared to magnetic fields encountered in laboratory environments, these fields play an important role in the dynamics of the ISM.

Magnetic fields influence the motion of charged particles and can affect the propagation of cosmic rays through the Galaxy. They also contribute to the pressure balance within the interstellar medium and can regulate the collapse of molecular clouds. Measurements of polarized radio emission and Faraday rotation provide important methods for studying Galactic magnetic fields.

The interstellar medium is therefore a highly dynamic environment shaped by the combined effects of gravity, turbulence, radiation, and magnetic fields. Energy injected into the ISM through stellar winds and supernova explosions drives large-scale turbulence and creates complex structures such as expanding shells and bubbles. These processes continuously redistribute energy and matter throughout the Galaxy.

Understanding the properties of the interstellar medium is essential for interpreting observations of Galactic radio emission. Many radio sources, including supernova remnants, H II regions, and diffuse synchrotron emission, arise from interactions between energetic particles and the interstellar medium. Consequently, studies of the ISM provide critical insights into the processes that govern star formation, cosmic ray acceleration, and the evolution of the Milky Way.

1.6 Radio Emission in the Galaxy

Radio astronomy has become one of the most powerful tools for studying the structure and physical processes occurring within the Milky Way (Condon and Ransom, 2016). Unlike optical radiation, radio waves are largely unaffected by interstellar dust and can therefore penetrate deep into the dense regions of the Galactic plane. This property makes radio observations particularly valuable for investigating star formation regions, supernova remnants, pulsars, and diffuse interstellar gas that would otherwise be obscured at shorter wavelengths (Wilson, Rohlfs, and Hüttemeister, 2013).

Radio emission in the Galaxy arises from a variety of physical mechanisms involving interactions between charged particles, magnetic fields, and ionized gas. Broadly speaking, Galactic radio emission can be divided into two main categories: thermal emission and non–thermal emission. Thermal emission is primarily associated with ionized gas in H II regions, while non–thermal emission is produced by relativistic particles moving in magnetic fields. These two types of emission have distinct spectral properties, allowing them to be distinguished through multi–frequency radio observations.

The fundamental quantity measured in radio astronomy is the specific intensity I_ν, which describes the amount of energy emitted per unit time, per unit frequency, per unit area, and per unit solid angle. In many cases it is convenient to express radio emission in terms of brightness temperature, defined through the Rayleigh–Jeans approximation of the Planck radiation law (Condon and Ransom, 2016). The brightness temperature T_b is given by

$$T_b = \frac{c^2}{2k\nu^2} I_\nu,$$

where c is the speed of light, k is Boltzmann's constant, and ν is the observing frequency. The brightness temperature provides a convenient way to compare radio emission from different astrophysical sources.

The propagation of radiation through the interstellar medium is governed by the radiative transfer equation (Rybicki and Lightman, 1979). In its simplest form, the change in specific intensity along a path length ds is given by

$$\frac{dI_\nu}{ds} = -\alpha_\nu I_\nu + j_\nu,$$

where α_ν is the absorption coefficient and j_ν is the emission coefficient. The first term represents the absorption of radiation by the medium, while the second term represents the generation of radiation by emission processes. The balance between these two terms determines the observed intensity of radio emission from astrophysical sources.

1.6.1 Thermal Free–Free Emission

One of the primary sources of radio emission in the Galaxy is thermal free–free emission, also known as bremsstrahlung radiation (Mezger and Henderson, 1967). This process occurs when free electrons are accelerated in the Coulomb fields of ions within an ionized plasma. Because the electrons are not bound to atoms before or after the interaction, the process is referred to as "free–free" emission.

Thermal free–free emission is commonly observed in H II regions surrounding young massive stars (Strömgren, 1939). Ultraviolet radiation from these stars ionizes the surrounding gas, producing a plasma consisting of electrons and protons. As electrons interact with ions, they emit radiation across a wide range of frequencies, including radio wavelengths.

The emissivity of thermal bremsstrahlung radiation can be expressed as

$$j_\nu \propto n_e^2 T^{-1/2} e^{-h\nu/kT},$$

where n_e is the electron density and T is the electron temperature. In the radio regime, where $h\nu \ll kT$, the exponential factor is approximately unity and the emission depends primarily on the square of the electron density (Rybicki and Lightman, 1979).

Thermal radio sources typically exhibit relatively flat spectra. The spectral index α, defined through the relation

$$S_\nu \propto \nu^\alpha,$$

is usually close to $\alpha \approx -0.1$ for optically thin free–free emission (Condon and Ransom, 2016). In optically thick regions, the spectral index can approach $\alpha \approx 2$. These spectral characteristics provide a useful diagnostic for distinguishing thermal sources from non-thermal radio emission.

1.6.2 Non–Thermal Synchrotron Emission

In addition to thermal emission, a significant fraction of the radio emission observed in the Galaxy arises from non-thermal processes. The most important of these processes is synchrotron radiation, which occurs when relativistic charged particles move through magnetic fields (Ginzburg and Syrovatskii, 1965).

When a charged particle travels through a magnetic field, it experiences a Lorentz force that causes it to spiral around magnetic field lines. The acceleration associated with this motion leads to the emission of electromagnetic radiation. For relativistic electrons, this radiation is referred to as synchrotron emission and can extend across a broad range of wavelengths from radio to X-rays.

The power radiated by a relativistic electron moving in a magnetic field can be expressed as

$$P \propto \gamma^2 B^2,$$

where γ is the Lorentz factor of the electron and B is the magnetic field strength. Because synchrotron radiation depends strongly on both the particle energy and the magnetic field, observations of synchrotron emission provide valuable information about cosmic rays and magnetic fields in the Galaxy (Ginzburg and Syrovatskii, 1965).

Synchrotron radiation typically produces a power–law spectrum. If the energy distribution of relativistic electrons follows a power law of the form

$$N(E) \propto E^{-p},$$

then the resulting synchrotron spectrum has a spectral index given by

$$\alpha = -\frac{p-1}{2}.$$

For many Galactic synchrotron sources, the spectral index lies in the range $\alpha \approx -0.5$ to -0.8. This steep spectral behaviour is a key signature of non-thermal emission (Dokara, Brunthaler, et al., 2021).

Synchrotron emission is also inherently polarised. Because relativistic electrons spiral around magnetic field lines, the emitted radiation exhibits a preferred orientation. Measurements of polarised radio emission therefore provide important information about the structure and orientation of magnetic fields within the Galaxy (Beck, 2015).

Non-thermal synchrotron radiation is observed in a wide range of astrophysical objects, including supernova remnants, pulsar wind nebulae, and diffuse Galactic emission (Reynolds, 2008). Supernova remnants, in particular, are among the strongest sources of synchrotron radiation in the Milky Way. In these objects, shock waves produced by supernova explosions accelerate charged particles to relativistic energies via diffusive shock acceleration (Bell, 1978).

Diffuse synchrotron emission is also observed throughout the Galactic disk and halo (Haslam et al., 1982). This emission arises from cosmic ray electrons interacting with large-scale Galactic magnetic fields. Observations of this diffuse radiation have provided important insight into the distribution of cosmic rays and magnetic fields in the Milky Way.

1.7 Spectral Index

The spectral index is one of the most important diagnostic tools used in radio astronomy (Condon and Ransom, 2016). As defined earlier, the flux density of a radio source varies with frequency according to the relation

$$S_\nu \propto \nu^\alpha,$$

where α is the spectral index. By measuring the flux density of a source at multiple frequencies, it is possible to determine the spectral index and thereby infer the dominant emission mechanism.

Thermal sources such as H II regions typically exhibit nearly flat spectra with $\alpha \approx -0.1$. In contrast, non-thermal synchrotron sources such as supernova remnants generally exhibit steeper spectra with α ranging from -0.3 to -0.8 (Ranasinghe and Leahy, 2023). Extremely steep spectra may indicate ageing populations of relativistic electrons or strong energy losses as a result of synchrotron cooling.

Spectral index mapping is therefore an essential technique in the study of Galactic radio sources (Beck, 2015). By analysing the spatial variation of the spectral index across an extended object, we can identify regions dominated by thermal or non-thermal emission. This method is particularly useful for distinguishing supernova remnants from H II regions in crowded regions of the Galactic plane.

Because many non-thermal sources exhibit stronger emission at low radio frequencies, observations at meter wavelengths are especially effective for detecting such objects (Roy and Rao, 2002a). Instruments such as the upgraded Giant Metrewave Radio

Telescope (uGMRT) provide high sensitivity and angular resolution at these frequencies, making them well-suited for studying synchrotron emission from Galactic sources (Gupta et al., 2017a).

In summary, radio emission in the Milky Way arises from a combination of thermal and non-thermal processes involving ionised gas, relativistic particles, and magnetic fields. Understanding these emission mechanisms is essential for interpreting radio observations of the Galactic plane and for identifying astrophysical sources such as supernova remnants and pulsars. The ability of radio observations to penetrate dense interstellar dust makes them an indispensable tool for exploring the complex and energetic environment of our Galaxy.

1.8 Supernova Remnants

Supernova remnants (SNRs) are among the most energetic and influential objects in the interstellar medium of galaxies. They are formed as a result of supernova explosions, which occur during the final stages of stellar evolution for certain types of stars. These explosions eject large amounts of material into the surrounding interstellar medium at velocities of several thousand kilometres per second, creating expanding shock waves that interact with the surrounding gas and magnetic fields. The resulting structures are known as supernova remnants (Reynolds, 2008).

Supernova explosions occur through two principal mechanisms. The first mechanism is the core-collapse supernova, which results from the gravitational collapse of massive stars with initial masses greater than approximately $8M_{\odot}$ (Woosley, Heger, and Weaver, 2002). When the nuclear fuel in the stellar core is exhausted, the core collapses under its own gravity, forming a neutron star or black hole and producing a powerful explosion that expels the outer layers of the star. The second mechanism is the thermonuclear or Type Ia, which occurs when a white dwarf in a binary system accretes matter from its companion star until it approaches the Chandrasekhar mass limit of approximately $1.4M_{\odot}$ (Hillebrandt and Niemeyer, 2000). At this point, runaway nuclear fusion reactions ignite and completely disrupt the star.

Regardless of the explosion mechanism, the expanding ejecta interact with the surrounding interstellar medium, producing a shock wave that compresses and heats the ambient gas. This interaction gives rise to a supernova remnant. The evolution of an SNR can be broadly divided into several distinct phases depending on the relative importance of the ejected mass, the swept-up interstellar medium, and radiative energy losses (Truelove and McKee, 1999).

The earliest stage of evolution is known as the free expansion phase. During this stage, the mass of the ejected material dominates over the mass of the swept-up interstellar medium. The ejecta expand nearly freely with velocities that may exceed 10^4 km s^{-1}. The radius of the expanding shell increases approximately linearly with time:

$$R(t) \approx v_0 t,$$

where v_0 is the initial expansion velocity. This phase typically lasts for several hundred years until the swept-up mass becomes comparable to the mass of the ejecta.

As the remnant expands further, it enters the adiabatic phase. In this stage, the mass of the swept-up interstellar medium exceeds the mass of the ejecta, and the expansion of the remnant is governed primarily by the conservation of energy. The evolution of the

shock radius during this phase can be described by the Sedov–Taylor solution (Sedov, 1959):

$$R(t) = \left(\frac{2.026Et^2}{\rho_0}\right)^{1/5},$$

where E is the energy released in the explosion, ρ_0 is the density of the ambient interstellar medium, and t is the time since the explosion. The Sedov–Taylor phase can last for tens of thousands of years and represents the stage during which most supernova remnants are observed.

During the Sedov phase, strong shock waves heat the surrounding gas to temperatures of several million Kelvin, producing thermal X-ray emission. At the same time, the shock front accelerates charged particles to relativistic energies via diffusive shock acceleration (Bell, 1978). In this mechanism, particles repeatedly cross the shock front and gain energy through interactions with magnetic turbulence. This process is believed to be one of the primary sources of Galactic cosmic rays (Blasi, 2013).

As the remnant continues to expand and cool, radiative energy losses become significant. The remnant then enters the radiative phase, also known as the snowplough phase (Cioffi, McKee, and Bertschinger, 1988). In this stage, the cooling of the shocked gas forms a thin, dense shell that sweeps up interstellar material as it expands. Eventually, the expansion slows, and the remnant gradually merges with the surrounding interstellar medium.

Supernova remnants are observed across the entire electromagnetic spectrum, from radio wavelengths to gamma rays (Reynolds, 2008). Each wavelength regime provides information about different physical processes occurring within the remnant. Radio observations are particularly important because most SNRs are strong sources of synchrotron radiation produced by relativistic electrons spiralling around magnetic field lines. The spectral index lies between -0.3 and -0.8, indicating that the emission is dominated by the synchrotron radiation of relativistic electrons (Ranasinghe and Leahy, 2023).

Morphologically, supernova remnants can be classified into several categories based on their radio appearance (Green, 2019). Shell-type remnants are the most common class and exhibit bright emission along the expanding shock front, forming a ring or shell-like structure. In contrast, plerionic remnants, also known as pulsar wind nebulae, are powered by the relativistic wind from a central pulsar and exhibit centrally filled radio emission (Gaensler and Slane, 2006). A third category, known as composite remnants, displays characteristics of both shell-type and plerionic structures.

The study of supernova remnants is important for several reasons. First, SNRs are major contributors to the energy budget of the interstellar medium. A typical supernova releases approximately 10^{51} ergs of energy (Chevalier, 1977), a significant fraction of which is transferred to the surrounding gas through shock waves. This energy injection drives turbulence in the interstellar medium and influences the dynamics of molecular clouds and star-forming regions.

Second, supernova remnants are believed to be the primary sites of cosmic ray acceleration in the Galaxy (Blasi, 2013). Observations of nonthermal radio emission and high-energy gamma rays from several SNRs provide strong evidence that particles are accelerated to relativistic energies in shock fronts. These cosmic rays play an important role in heating and ionising the interstellar medium.

Third, supernova explosions contribute to the chemical enrichment of galaxies (Woosley, Heger, and Weaver, 2002). Heavy elements synthesised in stellar interiors are ejected into the interstellar medium during the explosion and later incorporated into new generations of stars and planetary systems.

Despite their importance, the observed population of Galactic supernova remnants is significantly smaller than theoretical predictions. Based on estimates of the Galactic supernova rate, we expect the Milky Way to contain more than 1000 observable SNRs (Li et al., 1991). However, only a few hundred remnants have been confirmed observationally (Green, 2019). This discrepancy suggests that many remnants remain undetected, particularly in the crowded and highly obscured regions of the Galactic plane (Dokara, Brunthaler, et al., 2021).

Radio surveys of the Galactic plane play a critical role in identifying previously unknown supernova remnants. Because synchrotron emission from SNRs is often stronger at low radio frequencies, observations with instruments such as the upgraded Giant Metrewave Radio Telescope (uGMRT) are especially well suited for detecting faint and extended remnants (Gupta et al., 2017a). High-sensitivity radio imaging allows one to distinguish shell-like structures and measure spectral indices, providing key evidence for the identification of new SNR candidates.

The continued discovery and study of supernova remnants is therefore essential for improving our understanding of stellar evolution, cosmic-ray acceleration, and the interaction between massive stars and the interstellar medium. Radio observations remain one of the most effective tools for exploring these fascinating and energetic objects within the Milky Way.

1.9 High Energy Phenomena in the Galactic Center

The Galactic Centre hosts a wide range of high-energy astrophysical phenomena observed across X-ray and gamma-ray wavelengths. These emissions trace energetic processes associated with compact objects, particle acceleration, and large-scale outflows. At its core lies the supermassive black hole Sagittarius A* (Sgr A*), which exhibits variable X-ray and infrared emission, including flaring activity linked to processes in the accretion flow such as magnetic reconnection and particle acceleration. This region also contains a population of high-energy sources, including X-ray binaries, neutron stars, and stellar-mass black holes, along with diffuse X-ray emission from hot plasma at temperatures of several million kelvin, indicating strong energy injection into the interstellar medium. Gamma-ray observations reveal other energetic features, including the 511 KeV annihilation line and the large-scale Fermi bubbles extending $\sim$ 8 kpc above and below the Galactic plane . These structures are thought to originate from past activity of Sgr A* or collective effects of star formation and supernovae, with emission produced through inverse Compton scattering or hadronic processes (Su, Slatyer, and Finkbeiner, 2010). Radio observations further show that these structures are associated with magnetised plasma, while enhanced cosmic ray densities in the region contribute to interactions with the interstellar medium through ionisation and gamma-ray production.

1.10 Galactic Plane Radio Surveys

Large-scale galactic plane radio surveys have pushed ahead understanding of the structure and energetic processes occurring within the Milky way, because radio waves can

penetrate the dense interstellar dust that obscures optical observations, radio surveys provide a powerful means of studying objects embedded deep within the Galactic disk. Over the past several decades, many radio surveys have been conducted using both single dish telescopes and radio interferometers, producing detailed maps of the Galactic plane at a wide range of frequencies and angular resolutions.
One of the earliest and most widely used radio surveys is the NRAO VLA Sky Survey (NVSS) (Condon, W. D. Cotton, et al., 1998), which mapped a large portion of the sky at a frequency of 1.4 GHz using the Very Large Array (VLA). The NVSS survet achieved an angular resolution of approximately 45" and provided a comprehensive catalog of radio sources across the northern sky.
Another important survey is the Multi-Array Galactic Plane Imaging Survey (MAGPIS) (Dokara, Gong, et al., 2023), which focused specifically on the inner regions of the Galactic plane. MAGPIS utilised high-resolution VLA observations at 20 cm and provided detailed images of complex radio structures within the Galaxy. The improved sensitivity and angular resolution detailed images of complex radio structures within the Galaxy and also enabled the discovery of numerous previously unidentified supernova remnants and compact radio sources.
More recently, the THOR (The HI/OH/Recombination line survey, (Beuther et al., 2016)) survey has provided an extensive view of the Galactic plane at frequencies between approximately 1 and 2 GHz. This survey was conducted using the Karl G. Jansky Very Large Array, THOR combines continuum observation with spectral line data, allowing We to study both the distribution of interstellar gas and properties of radio continuum sources.
Some low-frequency radio observations have become important for studying non-thermal emission from Galactic sources. Instruments such as the Low Frequency Array (LOFAR, (Haarlem, Wise, Gunst, et al., 2013)) and Murchison Wide-field Array (MWA, (Tingay, Goeke, Bowman, et al., 2013)) have enabled high-sensitivity observations at frequencies below 300 MHz. At these low frequencies synchrotron emission from relativistic electrons becomes particularly prominent, making low-frequency surveys especially effective for detecting supernova remnants and other non thermal radio sources.
Some other major advancement in GC observations has come from MeerKAT radio telescope in South Africa. MeerKAT is a pioneer instrument for the Square Kilometre Array (SKA) and provides extremely high sensitivity and imaging quality. Observations conducted with MeerKAT have revealed a wealth of previously unseen structures in the inner galaxy, including filament radio features (Anderson et al., 2025). Despite these significant advances, the Galactic Plane remains one of the most challenging regions of the sky to observe. The high density of sources along the line of sight often leads to source confusion, making it difficult to distinguish individual objects from surrounding diffuse emission. Furthermore, extended radio sources such as supernova remnants may have low surface brightness and can therefore be difficult to detect in surveys with limited sensitivity.

Another challenge arises from the presence of strong background emission produced by diffuse synchrotron radiation from cosmic ray electrons interacting with Galactic magnetic fields. This diffuse emission can obscure faint structures and complicate the identification of individual sources. High dynamic range imaging and advanced data reduction techniques are therefore required to accurately characterise the radio emission from objects within the Galactic plane.

Low-frequency radio observations are particularly well suited for detecting faint and extended synchrotron sources. Because the flux density of synchrotron radiation typically increases toward lower frequencies, observations at meter wavelengths can reveal supernova remnants that may be difficult to detect at higher frequencies (Roy and Rao, 2002b). In addition, wide-field interferometers now allow We to image large regions of the Galactic plane with high sensitivity and angular resolution.

As a result, modern radio surveys continue to play a crucial role in expanding the known population of Galactic radio sources. In particular, many supernova remnants are believed to remain undiscovered, especially in the crowded and complex environments of the inner Galaxy. Improved observational capabilities therefore provide new opportunities for identifying previously unknown remnants and studying their physical properties.

1.11 Motivation for the Present Study

The Galactic Centre (GC) is one of the most dynamic and complex regions in the Milky Way, hosting a supermassive black hole, Sgr A*, with a mass of approximately $4 \times 10^6 M_\odot$ (Ghez et al., 2008; Gillessen et al., 2009). Despite its relative proximity compared to other galactic nuclei, the variability behaviour of Sgr A* at low radio frequencies remains poorly constrained. Understanding this variability is crucial for probing the accretion processes, jet activity, and the surrounding plasma environment near the central black hole (Bower, Markoff, et al., 2015).
Sgr A* is known to exhibit variability across multiple wavelengths, from near-infrared to X-ray, often associated with flaring activity (Baganoff et al., 2001; Genzel et al., 2003). At radio wavelengths, variability in Sgr A* can arise due to intrinsic emission changes as well as interstellar scattering effects, which are particularly pronounced at low frequencies (Bower, Falcke, et al., 2004). Multi-epoch low-frequency observations are therefore essential to disentangle intrinsic variability from propagation effects and to characterize the temporal behaviour of this source over time.

In addition to Sgr A*, the Galactic Centre region is populated by a remarkable network of non-thermal radio filaments, whose origin and emission mechanisms are still debated (Yusef-Zadeh, Hewitt, and W. Cotton, 2004). These filaments are typically associated with strong magnetic fields and are believed to trace relativistic electrons through synchrotron emission. However, in several cases, the observed spectral and morphological properties of filaments do not conform neatly to standard emission models, motivating further investigation at low radio frequencies where spectral diagnostics are most informative.

The upgraded Giant Metrewave Radio Telescope (uGMRT) provides an ideal facility for such a study. With its broad frequency coverage from ~120 MHz to 1.4 GHz, high sensitivity, and good *uv*-plane coverage, the uGMRT is well suited for both point source variability studies and the detection of extended diffuse structures (Gupta et al., 2017b). Observations in Band 4 (550–850 MHz) offer an effective balance between angular resolution and sensitivity, enabling in-band spectral index mapping alongside flux densit monitoring.

The present study is therefore motivated by two interconnected goals: first, to investigate the temporal variability of Sgr A* across multiple epochs at low radio frequencies; and second, to identify and characterize filamentary structures near the Galactic Centre through their spectral index properties and multi-wavelength counterparts. Together,

these objectives aim to advance our understanding of the emission processes and physical conditions in one of the most extreme environments in the Galaxy.

Chapter 2

Data Reduction and Processing

The data reduction process followed the workflow consisting of several key steps, each step used to transform raw observational data into scientifically usuable high-fidelity images. The pipeline encompasses environment setup data inspection, flagging, calibration, imaging, and self-calibration.

2.1 Setting up the Environment

First, start setting up the data processing environment. All data reduction tasks were performed on a Linux system via WSL (Windows Subsystem for Linux). The primary software package was CASA (Common Astronomy Software Applications; (The CASA Team et al., 2022)), which is the standard analysis environment for radio interferometric data. A Docker container was additionally configured to support wsclean ((Offringa et al., 2014), a wide-field deconvolution imager, and SAO-DS9 ((Joye and Mandel, 2003) for image inspection.

2.2 Data Inspection and Flagging

Before calibration, checked the raw visibility data thoroughly and identify and remove the corrupted, or unreliable measurements. This unreliable data could introduce errors and significant degrade in the quality of the final image (Thompson, Moran, and Swenson Jr., 2017).
Data inspection was done using CASA task. This LISTOBS task was used to obtain a comprehensive summary of the dataset, which had the information on the observed source, spectral windows, number of antennas, integration times, information of the telescope used for the observation etc., then detailed examination of the data was performed using PLOTMS task, which helped in the visualization of visibility, amplitudes and phases as functions of time, frequency, baseline length, and antenna pair.
By systematically examining amplitude variations across these axes, several common categories of data quality issues were identified:

- **Dead antennas**- Some antennas were found to be non-functional during specific scans, producing low or zero amplitudes. So data from such antennas were flagged entirely for the affected time period to prevent them from corrupting the calibration solutions.

- **Radio Frequency Interference (RFI)**- Disturbance from man-made electromagnetic signals detected in the data, manifesting as sharp spikes or irregular, non-astrophysical patterns (totally different from our dataset) in the amplitude-frequency or amplitude-time plots.

- **Scan edges**- Data recorded at the beginning and ending of the scans, corresponding to periods when the telescope is settling onto a source, were found to be unreliable and were accordingly flagged.

These issues were rectified using the task FLAGDATA in CASA, using this task, we could flag the data in both ways, manually and automatically. In Manual flagging- where specific antennas, time ranges, or frequency channels are explicitly selected for removal and in Automate flagging- task such as "tfcrop", which statistically detects and removes the outliers in the time-frequency plane (The CASA Team et al., 2022). This combined approach ensured the thorough removal of bad data while maximizing the retention of scientifically useful visibilities.

2.3 Calibration Workflow

In Calibration, as the raw visibilities are affected by a range of instrumental and atmospheric effects, including electronic gain drifts, delay offsets, bandpass variations, and ionospheric phase fluctuations ((Thompson, Moran, and Swenson Jr., 2017)). So before imaging, the calibration was performed in the following sequential manner:

- **Flux density calibration**- The absolute flux density scale was established using standard, well-characterized flux calibrtors such as 3C286, 3C48, 3C147, whose flux densities are known to high accuracy across a wide frequency range (Perley and Butler, 2013). The setjy task in CASA was used to set the model visibilities for these sources, providing the reference against which all subsequent calibration solutions are normalized.

- **Delay and Bandpass calibration**- Delay calibration was performed to correct for antenna-based timing offsets, which arise from differences in signal path lengths and instrumental delays across the array (Thompson, Moran, and Swenson Jr., 2017). Bandpass calibration subsequently accounted for the frequency-dependant gain response of each antenna, ensuring that the amplitude and phase response in uniform across all spectral channels.

- **Gain calibration**- Time-dependent variations in amplitude and phase, caused by drifts in the electronics and changes in atmospheric conditions over the course of the observation, were corrected through gain calibration. Solutions were derived at regular time intervals using a phase calibrator source located close to the target on the sky.

- **Applying calibration**- The derived calibration solutions were applied on the absolute flux scale using the FLUXSCALE task and also applied to the target source using APPLYCAL. The effectiveness of the calibration was verified by comparing the corrected and uncorrected visibility data using PLOTMS, confirm a significant reduction in scatter and improved coherence of the calibrated data.

2.4 Imaging and Self-Calibration

After the Calibration process, used the corrected column data to reconstruct the sky brightness distribution through the imaging process. Radio interferometric imaging involves Fourier inversion of the sampled visibilities, followed by deconvolution to account for the incomplete uv-plane coverage (Thompson, Moran, and Swenson Jr., 2017). The imaging and self-calibration procedure consisted of the following steps:

- **Splitting the target**- The calibrated data corresponding to the science target were first extracted into a separate Measurement set using the Split task. This step reduces the data volume and improves computational efficiency during subsequent imaging and self-calibration iterations.

- **Initial imaging**- An initial dirty image- representing the Fourier transform of the calibrated visibilities convolved with the synthesized beam- was first produced to assess the data quality and identify the extent of the emission. A cleaned image was subsequently generated using CASA's tclean algorithm, which applies the CLEAN deconvolution method to iteratively subtract the spread function from the image plane. The resulting image was inspected using IMVIEW to evaluate source morphology and image noise.

- **Self-calibration**- To further improve the fidelity of the image, an iterative self-calibration procedure was carried out (Cornwell and Wilkinson, 1981). Self-calibration uses the target source itself as a calibration reference, building a progressively more accurate sky model from successive imaging iterations. It works using the following steps:

- – A high-quality sky model was made using WSCLEAN (Offringa et al., 2014).
  – Gain corrections, which are derived by comparing the observed visibilities to the model using the GAINCAL task.
  – The derived corrections were applied to the data using APPLYCAL, and a new image was produced for the subsequent iteration.

Multiple self-calibration iterations were performed, with the early iterations restricted to phase-only corrections- which are more robust and less susceptible to overfitting- before progressing to joint amplitude and phase calibration in later cycles. This iterative approach progressively suppressed imaging artefacts, reduced the residual noise, and resulted in significantly improved image fidelity and sharper representation of the source structures. Multiple self-calibration iterations were performed, with the early iterations restricted to phase-only corrections — which are more robust and less susceptible to overfitting — before progressing to joint amplitude and phase calibration in later cycles. This iterative approach progressively suppressed imaging artefacts, reduced the residual noise, and resulted in significantly improved image fidelity and sharper representation of the source structures.

2.5 Pipeline-based processing

While manual data reduction is essential for understanding the workflow, it is inefficient for large datasets such as survey observations. Therefore, automated pipelines were also utilized. These pipelines integrate all processing steps—from flagging and calibration to imaging and self-calibration—into a single reproducible workflow. This ensures consistency across datasets and significantly improves processing efficiency, which is crucial for large-scale radio surveys.

2.6 *Wide-field Imaging with WSClean*

Although self-calibration is a standard step in the radio interferometric data reduction pipeline, but it was not applied in the present work due to the specific physical and observational challenges associated with the target field. Instead, Wise-field multi-scale imaging was carried out directly using WSCLEAN ((Offringa et al., 2014; Offringa and Smirnov, 2017)).

2.6.1 *Why Self-Calibration Was Not Applied*

The tarfet field is centred on the Galactic centre region, which contains Sgr A*, the supermassive black hole at the dynamical centre of the Milky way. Sgr A* lies behind a dense, turbulent ionised medium in the Galactic centre. At low radio frequencies, interstellar scattering dominates the observed structure of this source (Bower et al., 2006). The angular broadening due to scattering follows the frequency-dependent relation-

$$\theta_{\rm scatt} \propto \nu^{-2} \tag{2.1}$$

which results in strong angular broadening at the uGMRT observing frequencies (Gupta et al., 2017a). As a consequence, Sgr A* appears as an extended rather than a compact source, and exhibits significantly reduced surface brightness. Since self-calibration fundamentally requires a strong, well-defined compact source model as a reference, the extended and scatter-broadened appearance of Sgr A* renders it unsuitable for this purpose (Bower et al., 2014). Furthermore, the target region is embedded in an exceptionally complex astrophysical environment that includes multiple overlapping structures:

(a) **Sgr A West** — A prominent H II region immediately surrounding Sgr A*,

(b) **Sgr A East** — A supernova remnant in close projected proximity to the Galactic Centre, and

(c) **Diffuse Galactic Centre emission** — large-scale, extended continuum emission from the broader Galactic Centre environment.

At uGMRT frequencies, rapid phase fluctuations and direction-dependent effects dominate the interferometric response (Intema et al., 2009). These effects violate the fundamental assumption underlying standard self-calibration, namely that a single set of antenna-based phase corrections can sufficiently describe the calibration errors across the entire field of view. Consequently, applying self-calibration in this regime risks instability, potentially causing the algorithm to model and correct imaging artefacts rather than true antenna-based gain errors, thereby corrupting the final image rather than improving it.

2.6.2 *Wide-Field Multi-Scale Imaging*

Due to the limitations mentioned earlier, Used the multi-scale mode of WSCLEAN to create our radio images (Offringa and Smirnov, 2017). This approach is better at capturing emission structures of different sizes at the same time, and reduces imaging errors caused by the complex and extended emission in the Galactic Centre region.

Multi-scale WSCLEAN works by reconstructing both compact point-like sources and large diffuse structures simultaneously. This gives us a more accurate final image that faithfully represents the true brightness of the sky across all the different source sizes present in our data.

2.7 *Resolution-Tapered Imaging*

After the full-resolution images, a set of resolution-tapered images was made in order to enhance sensitivity to extended, low-surface-brightness emission structures that are partially or fully resolved out in the full-resolution maps. Tapering was applied by introducing a Gaussian weighting function in the uv-plane, which down-weighted the contributions from longer baselines during the imaging process (Thompson, Moran, and Swenson Jr., 2017).
From a physical condition, the angular resolution of a radio interferometer is determined by the maximum baseline length $b_{\max}$ in the array, according to the relation-

$$\theta_{\text{res}} \approx \frac{\lambda}{b_{\max}} \tag{2.2}$$

where λ is the observing wavelength (Thompson, Moran, and Swenson Jr., 2017).
While long baselines provide high angular resolution, they are also sensitive only to compact structures and are insensitive to emission that is more extended than the angular scale corresponding to the shortest baselines. By applying a Gaussian taper of 20-arcseconds in the uv-plane, the effective angular resolution of the image is reduced, suppressing the contribution of the longest baselines and thereby increasing the sensitivity to extended emission on scales up to the taper size. At the distance of the Galactic Centre ($\sim$ 8.2 kpc; GRAVITY Collaboration et al. 2019), an angular scale of 20 arcseconds corresponds to a physical scale of approximately 0.8 pc, which is well matched to the spatial scales of extended structures such as supernova remnant shells and large-scale non-thermal filaments expected in the Galactic Centre environment. The tapered images therefore, provide a complementary view of the field, revealing diffuse emission components that are suppressed in the full-resolution maps and enabling a more complete characterization of the total flux and morphology of extended sources.

2.8 *Contour Analysis and Multi-Wavelength Comparison*

Contour maps were produced to facilitate a detailed morphological examination of individual sources and extended structures within the Galactic Centre field. The contours were generated using the SAO-DS9, which allows interactive removal of intensity contour levels directly from the raio FITS images. The contour levels were set at multiples of the local rms noise level σ, ensuring that only statistically significant emission features are represented. These contours were subsequently exported and overlaid on images at complementary wavelengths, enabling a direct spatial comparison of the radio emission with emission observed at other frequency bands.

The physical motivation for this multi-wavelength comparison is rooted in the complementary nature of different observational wavebands for characterizing astrophysical emission mechanisms (M. Morris and Serabyn, 1996). Radio continuum emission at band-4 frequencies traces both thermal free-free emission from ionized gas in H II

regions and non-thermal synchrotron emission from relativistic electrons. In contrast, mid-infrared (MIR) emission primarily traces warm dust heated by young massive stars and is therefore closely associated with star-forming regions and thermal radio emitters. Near-infrared (NIR) emission is less affected by interstellar dust extinction than optical wavelengths and provides a relatively unobscured view of the underlying stellar population.

By overlaying radio contours on images at these complementary wavelengths, it becomes possible to classify individual radio sources based on the presence or absence of counterparts at other wavelengths. A spatial correlation between radio and MIR or NIR emission is indicative of a thermal origin, likely associated with H II regions or embedded star-forming activity, whereas radio sources lacking counterparts at these wavelengths are strong candidates for non-thermal emitters such as supernova remnants or pulsar wind nebulae (Condon and Ransom, 2016).

2.9 Primary Beam Correction

The response of a radio interferometric array is not spatially uniform across the field of view. Instead, the sensitivity of the array decreses with angular distance from the pointing center, following the primary beam pattern of the individual antennas (Thompson, Moran, and Swenson Jr., 2017). For the uGMRT at Band-4 frequencies, the primary beam response $A(\theta)$ can be approximated as a Gaussian function of the form

$$A(\theta) = \exp\left(-\frac{\theta^2}{2\sigma_{\rm pb}^2}\right) \tag{2.3}$$

where θ is the angular distance from the pointing centre and $\sigma_{\rm pb}$ is related to the full width at half maximum (FWHM) of the primary beam.

As a result of this spatially varying sensitivity, sources that are located farther away from the center of the image receive less sensitivity from the array compared to sources near the center. This means that in the uncorrected image, a source sitting near the edge of the field will appear fainter that it truly is, not because it is intrinsically faint, but simply because the antenna response is weaker at that position. If this effect is not corrected, then the measured flux densities of sources will depend on where they happen to fall within the image rather than on their true brightness. This would make any meaningful comparison of flux densities between sources at different positions, or any attempt to detect variability between two epochs, fundamentally unreliable. To correct for this effect, primary beam-corrected images were produced by dividing the output image from WSCLEAN by the modelled primary beam response of the uGMRT antennas at Band-4 frequencies (Gupta et al., 2017a). This correction restores the true flux densities of sources at all positions within field, ensuring that the measured flux densities are independent of the angular distance from the pointing center. It is important to note that the primary beam correction amplifies the noise level at positions away from the pointing center, since dividing by a small primary beam value magnifies both signal and noise equally. Consequently, the signal-to-noise (SNR) radio degrades toward the edge of the corrected image. In the context of the present work, the primary beam-corrected images were produced specifically to serve as the input data for the construction of difference maps. Since difference maps are constructed by substracting images obtained from

different observing epochs, it is essential that all input images are placed on a consistent and accurate flux scale across the entire field of view. Using uncorrected images for this purpose would introduce spurious spatial gradients in the difference maps that mimic variability but are purely instrumental in origin.

2.10 Difference Maps

One of the key scientific goals of this study is to investigate temporal variability in the radio emission from the Galactic Centre region. With five separate observing epochs available in the dataset, it is possible to construct difference maps by subtracting the primary beam-corrected image of one epoch from that of another. Since the radio emission from the vast majority of astrophysical sources in the Galactic Centre is not expected to vary significantly on short timescales, the difference map ideally should contain only noise. Any statistically significant residual emission in the difference map therefore provides direct evidence for temporal variability in the flux density of one or more sources within the field. Mathematically, the difference map $\mathcal{D}$ between two epochs i and j is defined as

$$\mathcal{D}_{ij} = I_i^{\mathrm{pb}} - I_j^{\mathrm{pb}} \tag{2.4}$$

where I_i^{pb} and I_j^{pb} are the primary beam-corrected images from epochs i and j, respectively. Positive residuals in $\mathcal{D}_{ij}$ indicate that a source was brighter during epoch i relative to epoch j, while negative residuals indicate the reverse. The noise level of the difference map σ_{diff} can be estimated as

$$\sigma_{\mathrm{diff}} = \sqrt{\sigma_i^2 + \sigma_j^2} \tag{2.5}$$

where σ_i and σ_j are the rms noise levels of the individual epoch images. A source is considered to show statistically significant variability if the peak residual in the difference map exceeds a threshold of $\sim 5\sigma_{\mathrm{diff}}$.

The physical significance of the difference maps in the context of the Galactic Centre field is particularly noteworthy. The region surrounding Sgr A* is known to host a variety of variable and transient radio sources, including X-ray binaries in outburst, magnetars, and flaring emission associated with the accretion flow onto the central supermassive black hole (Hyman et al., 2005; Eatough et al., 2013). Radio transients in this region can brighten by orders of magnitude over timescales ranging from hours to months.

2.11 Percentage Variation Maps

While the difference map provides an absolute measure of flux density variability, it does not account for the fact that the intrinsic brightness of sources varies considerably across the field. A faint source exhibiting a difference of 1 mJy beam^{-1} may represent a dramatic change in its flux density, whereas the same absolute difference for a bright source may be entirely insignificant. To address this limitation, a percentage variation map was constructed, which expresses the flux density change between two epochs as a fraction of the mean flux density of the source. The percentage variation map $\mathcal{P}_{ij}$ is

defined as

$$\mathcal{P}_{ij} = \frac{I_i^{\mathrm{pb}} - I_j^{\mathrm{pb}}}{\frac{1}{2}\left(I_i^{\mathrm{pb}} + I_j^{\mathrm{pb}}\right)} \times 100\% \tag{2.6}$$

This quantity provides a normalized, dimensionless measure of variability that is directly comparable across sources of different intrinsic brightnesses. Regions in the map where $|\mathcal{P}_{ij}|$ is large indicate sources whose flux density has changed significantly between the two epochs relative to their mean brightness, regardless of their absolute flux level. This makes the percentage variation map a particularly sensitive and physically meaningful diagnostic for identifying candidate variable sources within the complex and source-rich environment of the Galactic Centre. Together, the difference maps and percentage variation maps constitute a powerful and complementary pair of diagnostics for characterizing radio variability in the Galactic Centre field. The difference maps provide an absolute, noise-referenced measure of variability suitable for detecting strong transients, while the percentage variation maps provide a normalized perspective that highlights fractional changes in source brightness irrespective of source flux density.

Chapter 3

Results and Discussion

In this chapter, the radio continuum imaging results from uGMRT Band-4 (607.66 MHz) observations (Gupta et al., 2017a) of the Galactic Centre region. The analysis encompasses many results below, beginning with the full-field high-resolution images, followed by resolution-tapered images, contour cutout maps, difference maps, primary beam-correcred images, and lastly multi-wavelength overplot comparisons with optical and infrared data.

3.1 Full-Field Radio Continuum Maps

Figures below present the uGMRT Band 4 (550–850 MHz) radio continuum images (Gupta et al., 2017a) of the Galactic Centre field obtained across five observing epochs: 26 October, 14 November, 14 January, 22 February, and 01 April. Each image consists of 6000×6000 pixels with a pixel scale of 2 arcsec pixel^{-1}, covering a total field of view of approximately 3.3 deg $\times$3.3 deg centred on the Galactic Centre. The synthesised beam varies slightly across epochs, with BMAJ and BMIN ranging between approximately 6.95-9.92 arcsec and 5.15-5.96 arcsec, respectively, and a pixel size of 2.00 arcsec throughout. The colour scale in all images represents the intensity in units of Jy beam^{-1}, displayed using a logarithmic stretch to simultaneously highlight both the bright central emission and the faint extended structures across the field.

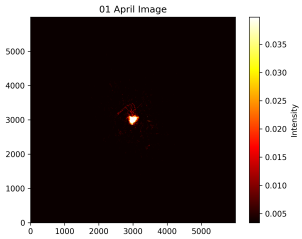

(3.1.1) 01 April

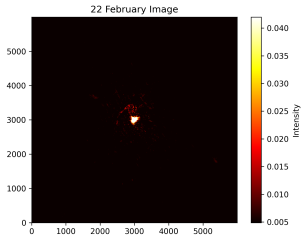

(3.1.2) 22 February

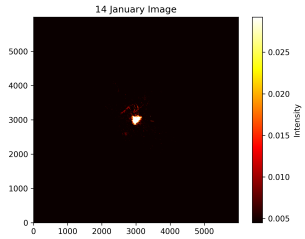

(3.1.3) 14 January

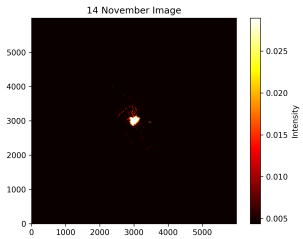

(3.1.4) 14 November

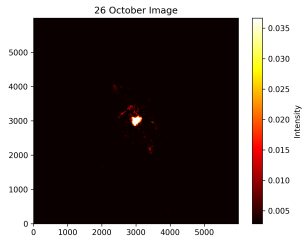

(3.1.5) 26 October

Figure 3.1: Full-field uGMRT Band 4 (550–850 MHz) radio continuum images of the Galactic Centre region across five observing epochs (3.13.1.1–3.13.1.5). The dominant central source is the Sgr A complex (Balick and Brown, 1974), visible as a bright compact structure near pixel coordinates (3000, 3000) in each epoch. Faint diffuse emission and extended radio structures are visible in the surrounding field.

The peak flux density of the central source, identified as the Sgr A complex (Balick and Brown, 1974) located at RA = 266.42 deg, Dec = −29.01 deg, varies across the five

epochs, with values of 0.793, 0.708, 0.546, 0.695, and 0.620 Jy beam^{-1} for 26 October, 14 November, 14 January, 22 February, and 01 April, respectively. The rms noise levels achieved in the five epochs are 0.945, 1.064, 1.047, 1.872, and 1.197 mJy beam^{-1} respectively, with 22 February showing a slightly elevated noise level compared to the other epochs, likely reflecting differences in the observing conditions or the amount of data flagged during that session.

In each of the five images, the vast majority of the 6000 × 6000 pixel field is devoid of significant radio emission, as expected for a field centred on the inner Galaxy at Band 4 frequencies. The emission is strongly concentrated toward the centre of the field, dominated by the Sgr A complex and the surrounding Galactic Centre environment (M. Morris and Serabyn, 1996). This spatial concentration reflects the true physical distribution of radio-emitting structures in the inner Galaxy, where the density of both thermal and non-thermal sources is extremely high within the central few degrees.

3.2 Central Region Cutout Maps

To examine the morphological details of the Galactic Centre emission more clearly, zoomed-in cutout images of the central ∼ 2000pixel×2000pixel region were extracted from the full-field maps. These cutouts, shown in the figures below, are displayed with proper World Coordinate System (WCS) axes in right ascension and declination, providing a physically meaningful spatial reference for the structures visible in the images.

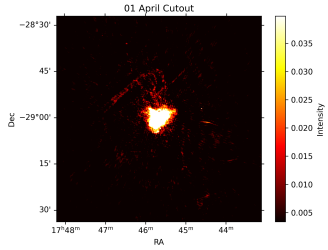

(3.2.1) 01 April

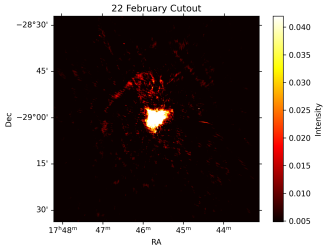

(3.2.2) 22 February

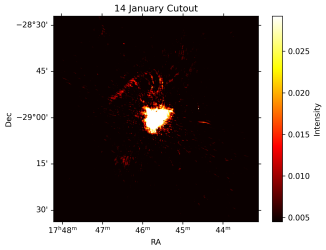

(3.2.3) 14 January

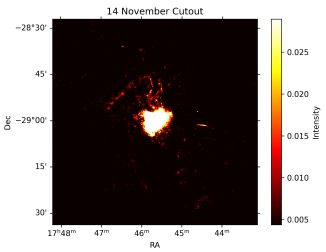

(3.2.4) 14 November

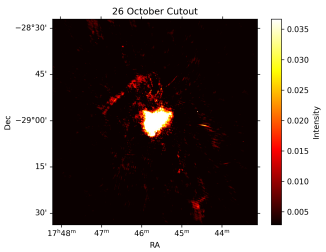

(3.2.5) 26 October

Figure 3.2: WCS-cutout images of the central Galactic Centre region extracted from the full-field uGMRT Band 4 maps for each of the five observing epochs. The field spans approximately 17^h44^m to 17^h48^m in right ascension and −2830′ to −2930′ in declination. The colour scale represents intensity in Jy beam^{-1}. The bright central source is the Sgr A complex, surrounded by a rich network of diffuse emission and non-thermal filamentary structures.

Zoomed-in field of view allow direct comparison with other published radio and multiwavelength observations of the Galactic Centre (Heywood et al., 2022). The

dominant feature in all five cutouts is the bright, saturated-appearing central source corresponding to the Sgr A complex, located at approximately $17^{h}45^{m}40^{s}$, −29 deg 00′. The apparent saturation of the central source in the colour scale is a display effect arising from the large dynamic range of the image, as the peak brightness of Sgr A far exceeds the brightness of the surrounding extended emission.

Surrounding the central source, all five epochs reveal a rich and complex network of extended radio emission extending across the field. The most prominent features visible in the cutout images are the following.

The bright, extended emission to the north and north-west of Sgr A, spanning declinations between approximately −28 deg 40′ and −28 deg 55′, traces the well-known non-thermal filamentary structures associated with the Galactic Centre Radio Arc (Yusef-Zadeh, M. Morris, and Chance, 1984). These filaments appear as elongated, thread-like structures oriented roughly perpendicular to the Galactic plane (Yusef-Zadeh, M. Morris, and Chance, 1984; Heywood et al., 2022), a characteristic morphology consistent with synchrotron emission from relativistic electrons spiralling along ordered magnetic field lines oriented perpendicular to the Galactic plane. The detection of these filaments at Band 4 frequencies is significant because synchrotron emission from such structures is brighter at lower radio frequencies, making uGMRT Band 4 an effective band for their characterisation (Yusef-Zadeh et al., 2022). Comparing the five cutout epochs, the overall morphology of the extended emission is broadly consistent, confirming that the large-scale structures detected are genuine astrophysical features and not imaging artefacts. However, subtle differences in the brightness and morphological detail of faint structures are visible between epochs, particularly in the 22 February image which shows somewhat enhanced diffuse emission across the field, consistent with its slightly elevated rms noise level. The January and April epochs show the cleanest representation of the filamentary structures to the north of the central source, with sharper delineation of individual filaments compared to the October and November epochs.

Table 3.1: Summary of uGMRT Band 4 full-field image parameters for each observing epoch. BMAJ and BMIN denote the major and minor axes of the synthesized beam respectively.

Epoch	BMAJ (arcsec)	BMIN (arcsec)	rms Noise (mJy beam^{-1})	Peak Flux (Jy beam^{-1})	Flux Range (Jy beam^{-1})
26 Oct	9.92	5.96	0.945	0.793	−0.025 to +0.793
14 Nov	7.42	5.15	1.064	0.708	−0.018 to +0.708
14 Jan	7.42	5.15	1.047	0.546	−0.017 to +0.546
22 Feb	7.25	5.72	1.872	0.695	−0.023 to +0.695
01 Apr	6.95	5.91	1.197	0.620	−0.021 to +0.620

3.3 Resolution-Tapered Images

To recover extended low-surface-brightness emission that is partially or fully resolved out in the full-resolution maps, resolution-tapered images were produced for all five observing epochs. Tapering was implemented in Python using the `python-casacore` and `WSClean` (Offringa et al., 2014) imaging pipeline, in which a Gaussian taper of 20 arcseconds was applied in the *uv*-plane prior to imaging. Specifically, the taper was introduced by passing the parameter `-taper-gaussian 20asec` to the WSCLEAN call within the

Python script, which applies a Gaussian weighting function $W(u, v) = \exp\left(-\frac{u^2+v^2}{2\sigma^2_{\text{taper}}}\right)$ to the visibility weights in the uv-plane, thereby down-weighting contributions from longer baselines and reducing the effective angular resolution of the resulting image. From the fundamental relation between angular resolution and baseline length,

$$\theta_{\text{res}} \approx \frac{\lambda}{b_{\text{max}}}, \tag{3.1}$$

applying the 20-arcsecond taper effectively suppresses the response to structures smaller than this angular scale while enhancing sensitivity to emission extended over larger angular scales (Thompson, Moran, and Swenson Jr., 2017). At the distance of the Galactic Centre ($\sim$ 8.2 kpc; GRAVITY Collaboration et al. 2019), a 20-arcsecond angular scale corresponds to a physical scale of approximately 0.8 pc, which is well matched to the spatial extent of extended structures such as non-thermal filaments and diffuse synchrotron emission expected in the Galactic Centre environment (Yusef-Zadeh, M. Morris, and Chance, 1984; Heywood et al., 2019). Two complementary views are presented for each epoch: a full-field image covering the complete $\sim 3.3^\circ \times 3.3^\circ$ field of view, and a zoomed-in cutout image centred on the Sgr A complex covering the central $\sim 2000 \times 2000$ pixel region.

3.3.1 Full-Field Tapered Images

Figures 3.3.1 present the full-field resolution-tapered images for the 01 April, 22 February, 26 October, 14 January, and 14 November epochs respectively. Each image covers the complete 6000×6000 pixel field of view with a 2 arcsecond pixel scale. The colour scale represents intensity in units of Jy beam^{-1}.

In all five full-field tapered images, the emission is strongly concentrated toward the Galactic Centre, with the Sgr A complex appearing as a bright, slightly extended source near pixel coordinates $(3000, 3000)$. The peak intensity in the full-field tapered images is substantially elevated compared to the corresponding full-resolution maps, reaching values of approximately 0.5 Jy beam^{-1} in the 14 January and 14 November epochs. This enhancement arises directly from the increased synthesised beam area produced by the tapering: by collecting flux from a larger solid angle into each beam, the per-beam intensity is amplified relative to the full-resolution case. Faint extended emission surrounding the central source is also visible in several epochs, particularly in the 26 October and 22 February full-field tapered maps, where a diffuse emission component extending to the north-west of the central source is recovered that is not visible in the full-resolution full-field maps. This is consistent with the presence of large-scale diffuse synchrotron emission in the inner Galaxy that is resolved out at full resolution (Heywood et al., 2019).

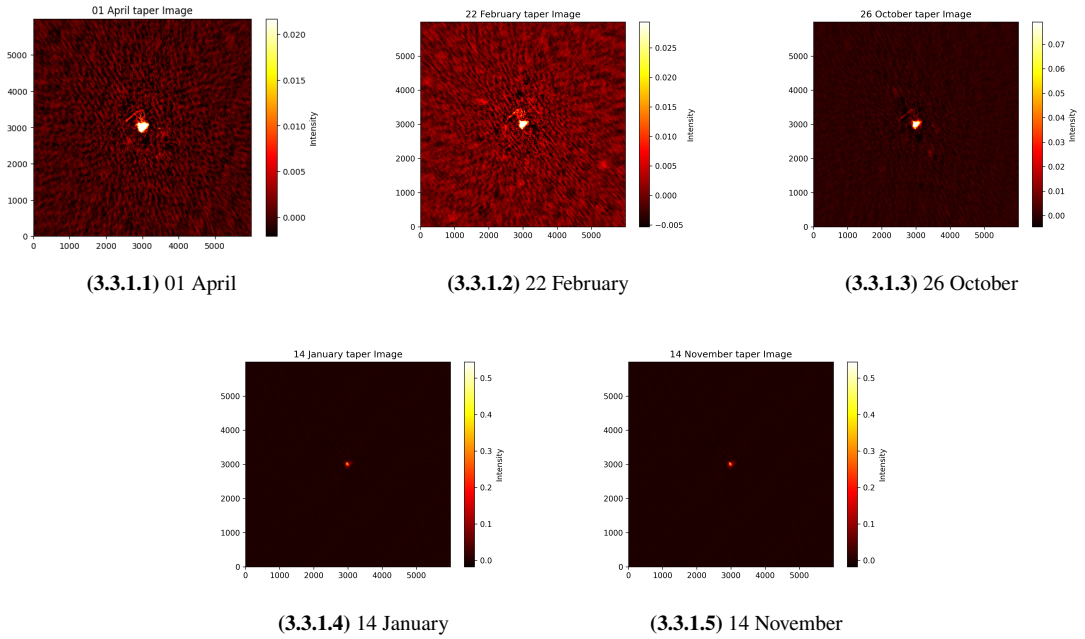

(3.3.1.1) 01 April **(3.3.1.2)** 22 February **(3.3.1.3)** 26 October

(3.3.1.4) 14 January **(3.3.1.5)** 14 November

Figure 3.3.1: Full-field resolution-tapered (20-arcsecond *uv*-taper) images of the Galactic Centre region for all five observing epochs. The Sgr A complex is visible as the bright compact structure near pixel coordinates (3000, 3000) in each epoch. The colour scale represents intensity in Jy beam^{-1}.

The full-field tapered images for the 14 January and 14 November epochs show the highest peak intensities among all five epochs, with values reaching ~ 0.5 Jy beam^{-1}, consistent with the behaviour observed in the full-resolution maps where these epochs also exhibit relatively high peak flux densities. In contrast, the 01 April and 26 October full-field tapered maps show peak intensities of approximately 0.020–0.025 Jy beam^{-1}, notably lower than the January and November epochs. This epoch-to-epoch variation in the tapered full-field maps is broadly consistent with the flux variability identified from the primary beam corrected light curve (Section 3.4), and reflects a combination of genuine source variability, differences in *uv*-coverage between epochs, and the amount of extended flux recovered by the respective synthesised beams.

3.3.2 Cutout Tapered Images

Figures 3.3.2 present the resolution-tapered cutout images for the five epochs. Each cutout is centred on the Sgr A complex and covers approximately 17×17 arcmin, displayed with proper World Coordinate System (WCS) axes in right ascension and declination. The colour scale represents intensity in Jy beam^{-1} with the intensity range typically spanning 0–0.020 Jy beam^{-1} across most epochs.

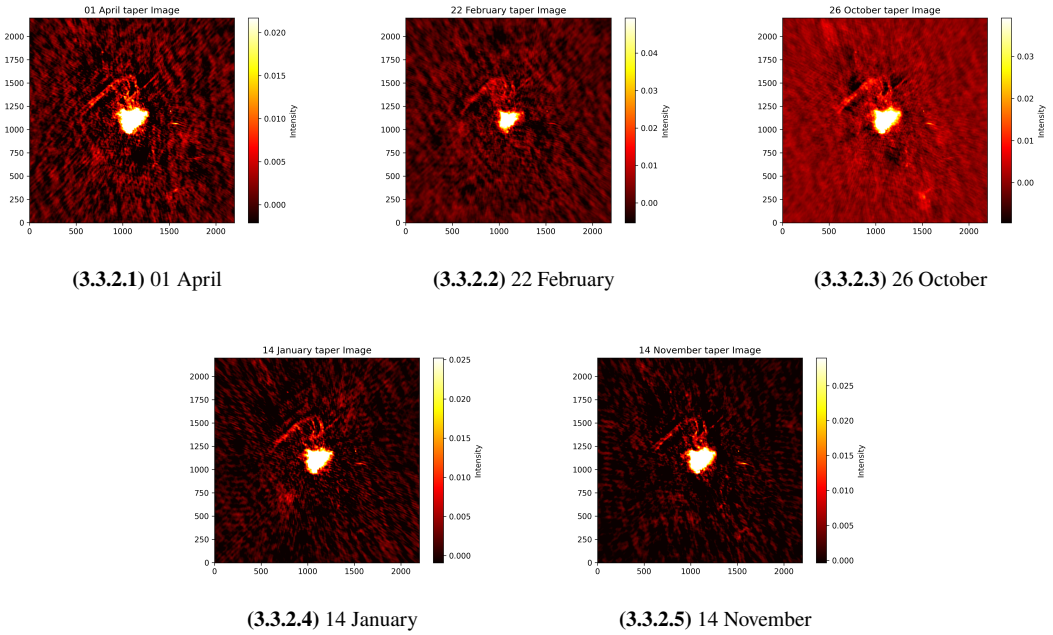

(3.3.2.1) 01 April **(3.3.2.2)** 22 February **(3.3.2.3)** 26 October

(3.3.2.4) 14 January **(3.3.2.5)** 14 November

Figure 3.3.2: Resolution-tapered (20-arcsecond *uv*-taper) cutout images of the central Galactic Centre region for all five observing epochs. The field is centred on the Sgr A complex. The colour scale represents intensity in Jy beam^{-1}. Extended diffuse emission and filamentary structures to the north of the central source are prominently recovered compared to the full-resolution cutout maps.

The tapered cutout images reveal considerably more extended diffuse emission surrounding the bright central Sgr A complex than is visible in the corresponding full-resolution cutout maps (Section 3.2). The dominant feature in all five tapered cutout images is the bright central source associated with the Sgr A complex. However, a rich network of diffuse and filamentary emission is now prominently recovered across the surrounding field. In particular, the extended emission to the north and north-west of the Sgr A complex, associated with the non-thermal filamentary structures of the Galactic Centre Radio Arc (Yusef-Zadeh, M. Morris, and Chance, 1984), is recovered with enhanced brightness and spatial continuity in the tapered maps. A prominent elongated emission feature extending from Sgr A toward the north is clearly visible in the 01 April and 14 January tapered cutout images, which is interpreted as emission associated with the Radio Arc filaments (Yusef-Zadeh, M. Morris, and Chance, 1984; Heywood et al., 2022). These filaments appear morphologically broader and smoother compared to the full-resolution maps, as expected given the reduced angular resolution imposed by the taper, but their overall large-scale structure and orientation are preserved.

Comparing the five tapered cutout epochs, the overall morphology of the extended emission is broadly consistent across observations, confirming that the recovered diffuse structures are genuine astrophysical features and not imaging artefacts introduced by the tapering. However, notable differences in the prominence of the extended emission are visible between epochs. The 01 April and 22 February tapered cutout images show relatively more extended diffuse emission throughout the field, while the 14 November epoch displays a somewhat more compact morphology. The 22 February tapered cutout image also shows enhanced diffuse emission across the field consistent with its elevated image noise level of $\sigma \approx 1.872$ mJy beam^{-1} (Table 3.1), where noise contributions at low intensity levels are amplified by the tapering process.

The tapered images also reveal a faint elongated emission structure extending toward

the south of the Sgr A complex in the 26 October and 14 November cutout tapered maps that is not present in the full-resolution cutout images. This structure is likely associated with diffuse extended emission from the Galactic Centre environment (M. Morris and Serabyn, 1996) and demonstrates that the 20-arcsecond taper is effective at recovering emission on scales of $\sim$ 1 pc that would otherwise be resolved out at the full resolution of the uGMRT Band 4 observations. Taken together, the full-field and cutout tapered images confirm that a 20-arcsecond uv-plane taper, applied through the Python-based imaging pipeline, provides a powerful complementary view of the Galactic Centre field, recovering diffuse emission structures that are suppressed in the full-resolution maps and enabling a more complete characterisation of the total radio emission present in this complex astrophysical environment.

3.4 Primary Beam Corrected Images and Light Curve of the Central Source

Before constructing the light curve, primary beam corrected images were produced for all five observing epochs.The sensitivity of the uGMRT array (Gupta et al., 2017a) decreases with increasing angular distance from the pointing centre, following the primary beam response pattern of the antennas. In the uncorrected images, this causes sources away from the phase centre to appear artificially fainter than they truly are. To recover the true flux densities across the full field of view, each epoch image was divided by the modelled primary beam response of the uGMRT at Band 4 frequencies, producing a set of primary beam corrected FITS images. These corrected images place all sources across the field on a consistent and accurate absolute flux scale, independent of their angular distance from the pointing centre, and were used as the direct input for all subsequent flux density measurements and variability analysis.

Using these primary beam corrected images, a light curve of the central Galactic Centre region was constructed by measuring the integrated flux density within a fixed aperture centred at pixel position (x = 3000, y = 3000) across all five epochs. This aperture encompasses not only the location of Sgr A* but also the surrounding extended emission — including Sgr A West (the H II region), Sgr A East (the supernova remnant), and diffuse continuum emission from the broader Galactic Centre environment (M. Morris and Serabyn, 1996) — and therefore measures the total integrated flux density of the central Galactic Centre complex as a whole. The resulting light curve is presented in Figure 3.3.2.

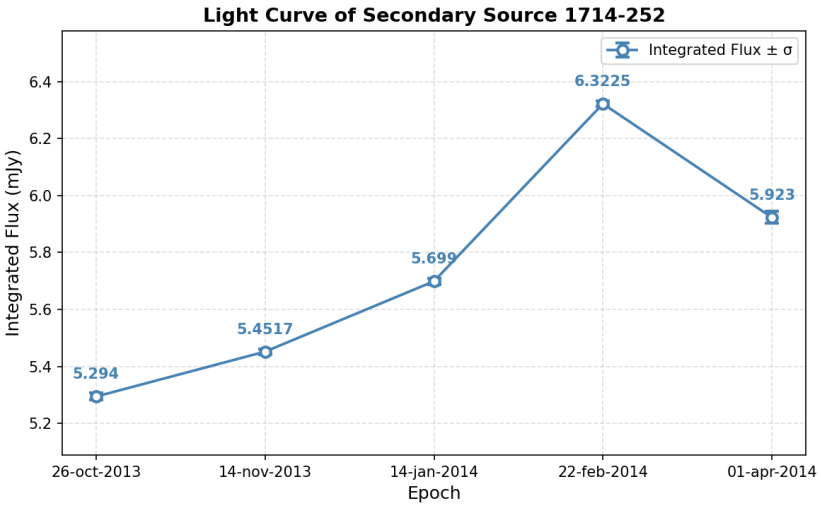

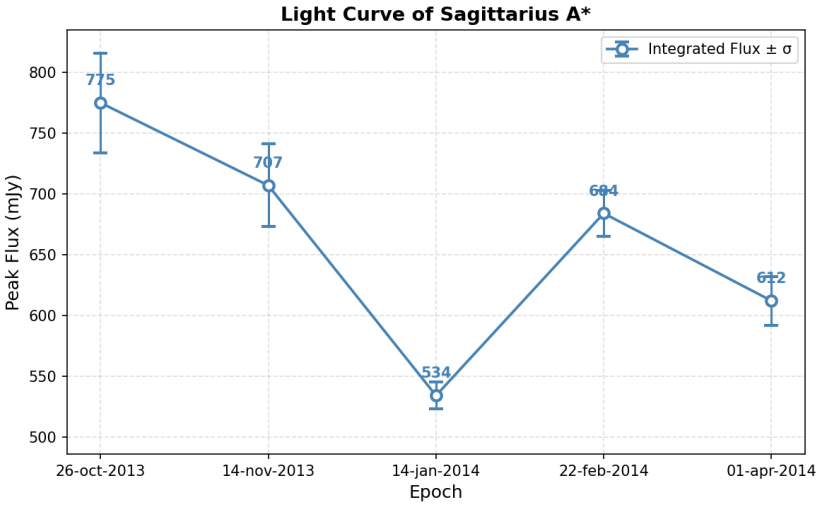

Figure 3.3.2: Light curve of the integrated flux density measured at the fixed pixel position ($x = 3001$, $y = 3001$) using a compact aperture centred on the location of Sgr A*, constructed from the primary beam corrected uGMRT Band 4 images across the five observing epochs. The x-axis shows the observation date extracted from the FITS headers (DATE-OBS) and the y-axis shows the integrated flux density in mJy. Error bars represent $\pm\,\sigma_{\rm rms}$ of each epoch image. The flux densities lie in the range $\sim$534–775 mJy, with an apparent peak during the 14 January epoch (Roy and Pramesh Rao, 2004). However, as discussed in the text, at Band 4 frequencies Sgr A* is heavily scatter-broadened by the intervening ionised medium (Bower et al., 2006) and cannot be cleanly isolated from the surrounding extended emission. The epoch-to-epoch variation visible here is therefore attributed primarily to imaging systematics — including beam size differences, uv-coverage variations, and residual calibration offsets between epochs — rather than to genuine intrinsic variability of Sgr A* itself.

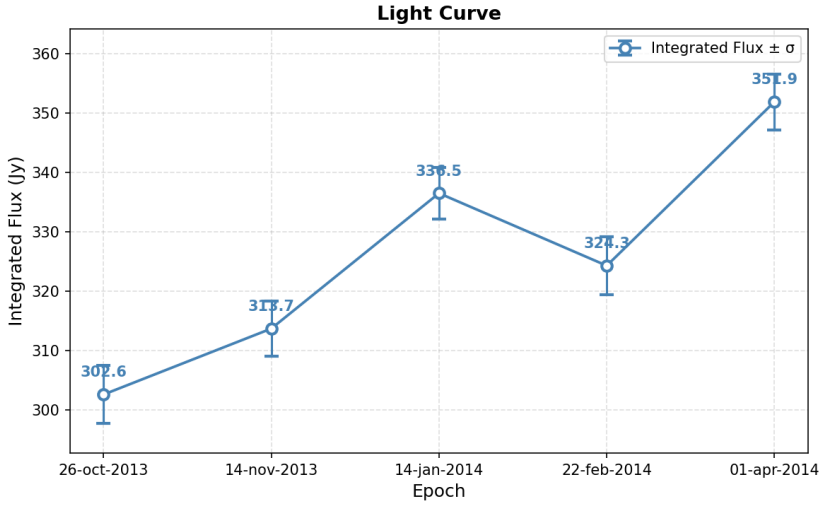

Figure 3.3.2: Light curve of the integrated flux density of the central Galactic Centre region (Sagittarius A complex), measured from the primary beam corrected uGMRT Band 4 images across the five observing epochs. The aperture is centred at pixel position ($x = 3001$, $y = 3001$) and encompasses the Sgr A complex together with the surrounding extended emission. The x-axis shows the observation date extracted from the FITS headers (DATE-OBS) and the y-axis shows the integrated flux density in Jy. The flux densities lie in the range $\sim$ 303–352 Jy, consistent with the known total radio flux of the Galactic Centre complex at Band 4 frequencies. A local minimum is visible during the 22 February epoch, while the 01 April epoch shows the highest recovered flux.

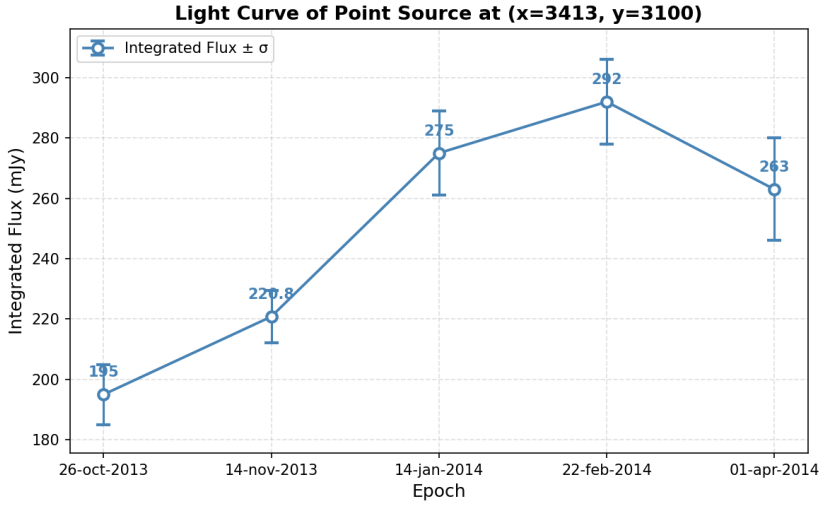

Since the uncorrected images have a spatially varying sensitivity pattern, any flux density measurement made directly from them would be biased by the position-dependent primary beam attenuation. By using the primary beam corrected images instead, the measured flux densities are free from this instrumental bias, and any epoch-to-epoch variations in the measured flux. The y-axis of the light curve shows the integrated flux density in units of Jy, which is distinct from the peak flux density in Jy beam^{-1} seen in the image colour scales. The integrated flux density is obtained by summing the flux contributions from all pixels within the defined aperture and converting from Jy beam^{-1} to Jy by accounting for the synthesised beam area. The resulting integrated flux values in the range $\sim$ 303–352 Jy are entirely physically consistent with the known total radio flux density of the Galactic Centre complex at Band 4 frequencies,

which has been reported to be of the order of hundreds of Jy in previous studies of this region (M. Morris and Serabyn, 1996).

The light curve reveals epoch-to-epoch variation in the recovered integrated flux density of the central region. The total range across the five epochs is approximately 49 Jy, corresponding to a fractional variation of roughly 15% relative to the mean flux level.

It is important to note, however, that this epoch-to-epoch variation cannot be straightforwardly attributed to genuine astrophysical variability of the sources within the field. Several instrumental and imaging effects are expected to contribute significantly to the observed flux differences:

- **Synthesised beam size variations-** The synthesised beam dimensions vary across epochs (BMAJ and BMIN range between approximately 6.95-9.92 arcsec and 5.15-5.96 arcsec respectively; Table 3.1). Since the integrated flux is computed by accounting for the beam area, differences in the beam size between epochs directly affect the fraction of extended emission recovered at each epoch.

- **UV-coverage differences-** Each epoch has a different uv-plane sampling pattern depending on the hour-angle coverage and the amount of data flagged during that session. This affects the angular scales of emission that are recovered in the image, and therefore the total integrated flux measured within the aperture.

- **Calibration differences-** In the absence of self-calibration — which was not applied in this work due to the complexity of the Galactic Centre field - residual gain errors between epochs may introduce systematic offsets in the absolute flux scale of each image.

It is also worth noting that Sgr A*, the compact supermassive black hole at the dynamical centre of the Galaxy, is not expected to be a significant source of variability at Band 4 frequencies on the timescales probed here. At these low radio frequencies, the observed emission from Sgr A* is heavily dominated by interstellar scattering, which broadens the source angularly and effectively smears any intrinsic flux variations into the surrounding diffuse emission (Bower et al., 2006). The scattering angular size scales as $\theta_{\rm scatt} \propto \nu^{-2}$, so at Band 4 frequencies the scatter-broadened size of Sgr A* is large enough that it cannot be cleanly separated from the surrounding extended structures in these images. Consequently, the measured integrated flux at the central position reflects the collective emission of the entire Galactic Centre complex rather than the intrinsic variability of Sgr A* alone.

The observed flux variation in Figure 3.3.2 should therefore be interpreted as an upper limit on any genuine astrophysical variability in the central Galactic Centre region, with the understanding that imaging systematics — particularly beam size and uv-coverage differences — likely account for a substantial fraction of the observed epoch-to-epoch flux changes. A proper characterisation of genuine variability in this field would require self-calibration, matched uv-plane weighting across all epochs. The light curve nonetheless motivates the construction of difference maps and percentage variation maps presented in the following sections, which provide a more spatially resolved view of the flux changes across the field.

3.5 *Difference Maps*

Difference maps were constructed for all ten unique epoch-pair combinations from the five uGMRT Band 4 observations, following $\mathcal{D}_{ij} = I_i^{\mathrm{pb}} - I_j^{\mathrm{pb}}$, where I_i^{pb} and I_j^{pb} are the primary-beam-corrected images of epochs i and j respectively. Each map covers the central 2000×2000 pixel subregion (pixel range 2000–4000 in both axes) of the full 6000×6000 pixel field, displayed on a symmetric logarithmic colour scale spanning $\pm 10^{-2}$ to $\pm 10^{-1}$ Jy beam^{-1}, with positive residuals (first epoch brighter) in yellow-green and negative residuals (second epoch brighter) in blue-purple.

All ten maps show a radial spoke-like pattern of alternating positive and negative residuals emanating from the central Sgr A region near pixel (3000, 3000). This arises from the mismatch of synthesised beam sidelobe structures between epochs, since beam shape and orientation vary with hour-angle coverage, flagging history, and parallactic angle rotation (Thompson, Moran, and Swenson Jr., 2017). As self-calibration was not applied (Section 2.6; Cornwell and Wilkinson 1981), phase errors from the bright central source are present in each image and contribute to this residual structure. In every map, the central region near the Sgr A complex appears as a dark core with near-zero residuals, as the dominant bright central emission largely cancels in the subtraction.

26 Oct − 14 Nov

Figure 3.3.2 shows the 26 Oct − 14 Nov difference map. This map shows the finest and densest radial streak structure among all ten pairs. The field is dominated by green (small positive) residuals throughout, with no large-scale coherent positive or negative patches visible beyond the radial artefact structure.

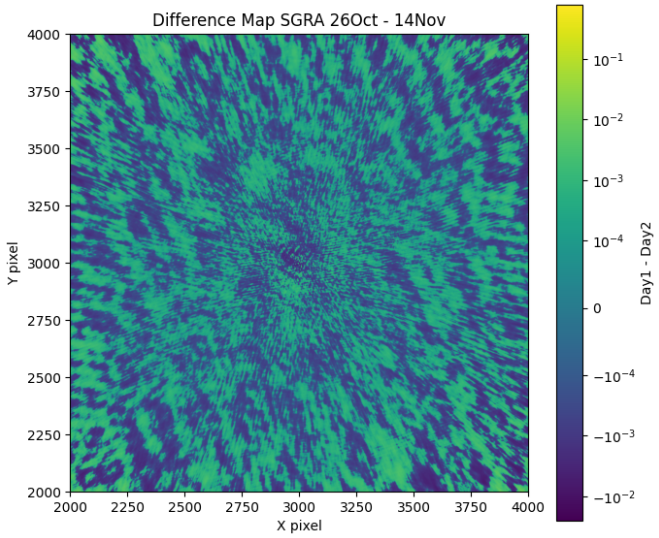

Figure 3.3.2: Difference map for the epoch pair 26 Oct − 14 Nov. The colour scale is symmetric logarithmic spanning $\pm 10^{-2}$ to $\pm 10^{-1}$ Jy beam^{-1}. Positive residuals (26 Oct brighter) are shown in yellow-green and negative residuals (14 Nov brighter) in blue-purple.

26 Oct − 14 Jan

Figure 3.3.2 shows the 26 Oct − 14 Jan difference map. The inner region of the field is broadly green-positive, while blue-purple tones become progressively more prominent

toward the outer corners, indicating that the 14 Jan epoch recovers greater flux in the outer regions of the field relative to 26 Oct.

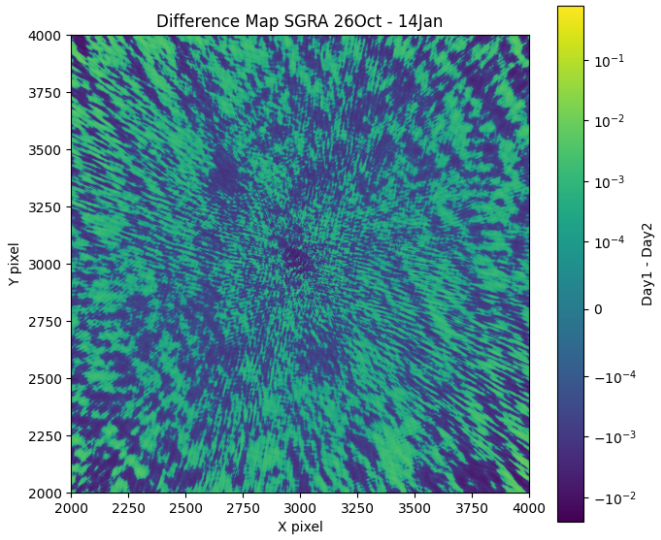

Figure 3.3.2: Difference map for the epoch pair 26 Oct − 14 Jan. Colour scale as in Figure 3.3.2.

26 Oct − 22 Feb

Figure 3.3.2 shows the 26 Oct − 22 Feb difference map. Large-scale coherent blue-purple patches are visible across significant portions of the outer field, indicating that the 22 Feb epoch is brighter than 26 Oct in those regions. These patches are more spatially extended than the radial sidelobe artefacts and represent the most prominent negative residuals seen in any pair involving the 26 Oct epoch.

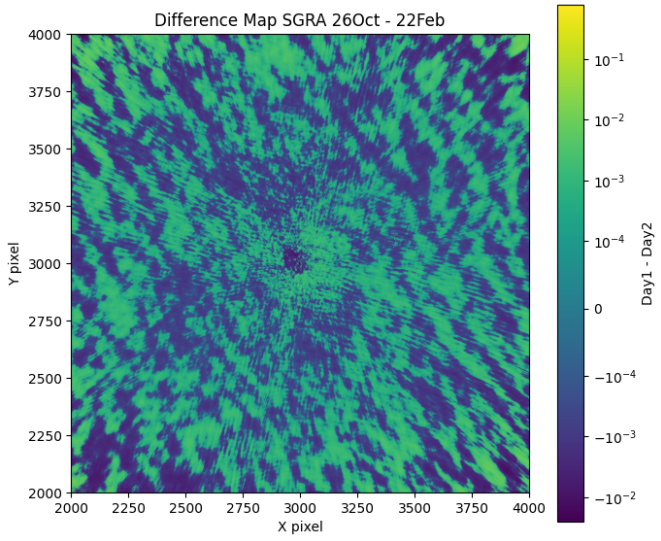

Figure 3.3.2: Difference map for the epoch pair 26 Oct − 22 Feb. Colour scale as in Figure 3.3.2.

26 Oct − 01 Apr

Figure 3.3.2 shows the 26 Oct − 01 Apr difference map. The field is predominantly green with a moderately uniform radial artefact pattern, indicating that the 26 Oct epoch

is generally brighter than 01 Apr across most of the field. No prominent large-scale coherent patches are visible.

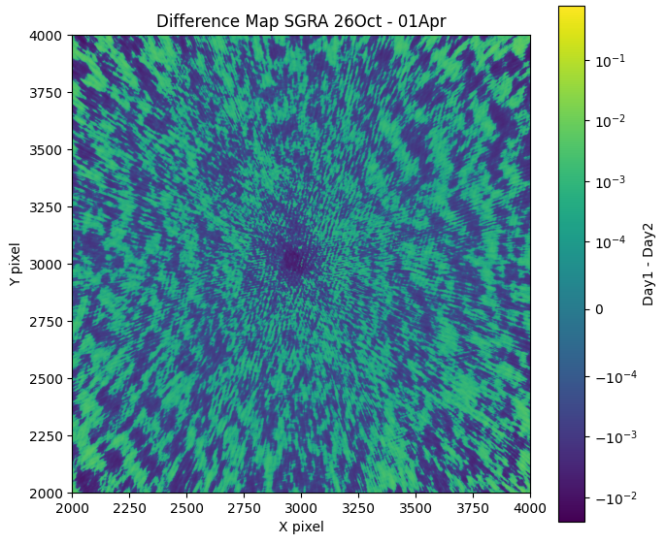

Figure 3.3.2: Difference map for the epoch pair 26 Oct − 01 Apr. Colour scale as in Figure 3.3.2.

14 Nov − 14 Jan

Figure 3.3.2 shows the 14 Nov − 14 Jan difference map. The outer field shows increased blue-purple tone relative to the 26 Oct − 14 Nov map, with coherent negative patches more clearly visible, indicating higher flux levels in the 14 Jan epoch compared to 14 Nov in the outer regions.

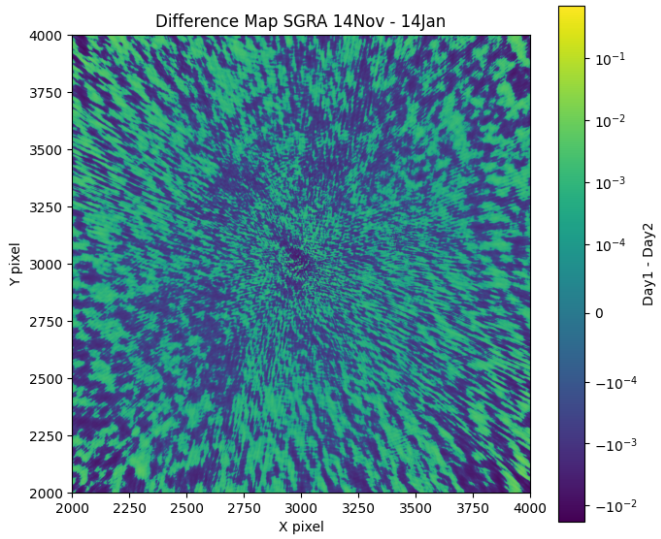

Figure 3.3.2: Difference map for the epoch pair 14 Nov − 14 Jan. Colour scale as in Figure 3.3.2.

14 Nov − 22 Feb

Figure 3.3.2 shows the 14 Nov − 22 Feb difference map. This map shows the most extensive blue-purple outer field among all pairs involving 14 Nov. Large coherent negative patches extend across a substantial portion of the field, indicating that 22 Feb

is brighter than 14 Nov over extended spatial scales. The negative residuals here are comparable in spatial extent to those seen in the 26 Oct – 22 Feb map.

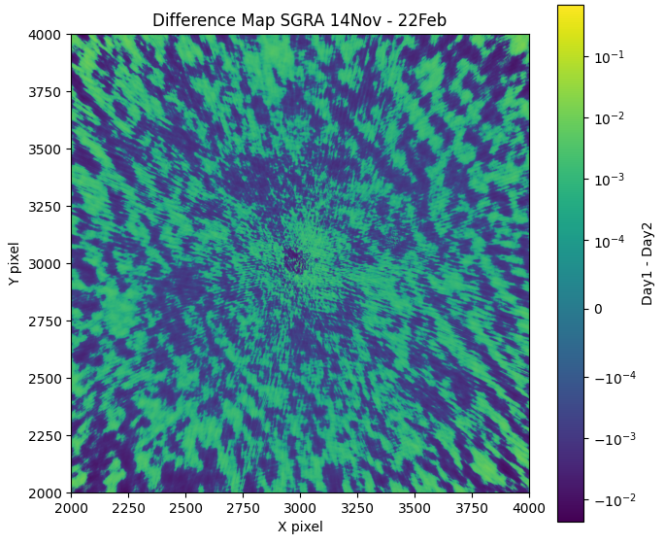

Figure 3.3.2: Difference map for the epoch pair 14 Nov – 22 Feb. Colour scale as in Figure 3.3.2.

14 Nov – 01 Apr

Figure 3.3.2 shows the 14 Nov – 01 Apr difference map. The field is predominantly green with a prominent radial sidelobe pattern. No large-scale coherent positive or negative features are apparent, indicating broadly similar flux levels between these two epochs across the field.

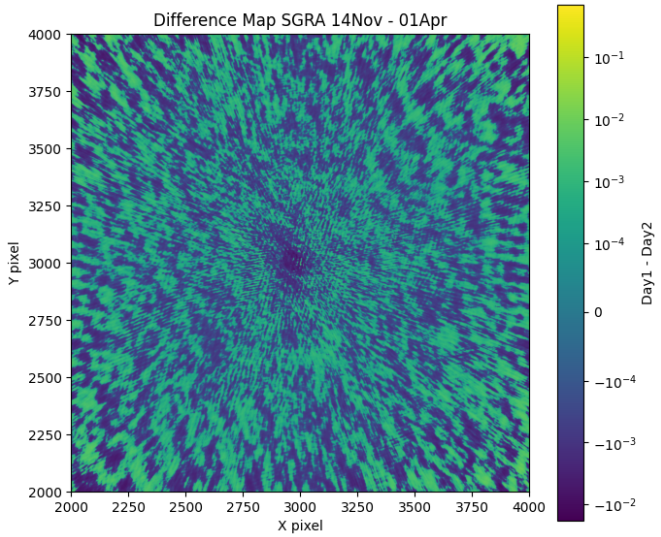

Figure 3.3.2: Difference map for the epoch pair 14 Nov – 01 Apr. Colour scale as in Figure 3.3.2.

14 Jan – 22 Feb

Figure 3.3.2 shows the 14 Jan – 22 Feb difference map. Strong blue-purple patches are visible in the outer field, consistent with 22 Feb being brighter than 14 Jan in the

extended emission regions. The inner region near the Sgr A complex retains the dark central core seen in all maps.

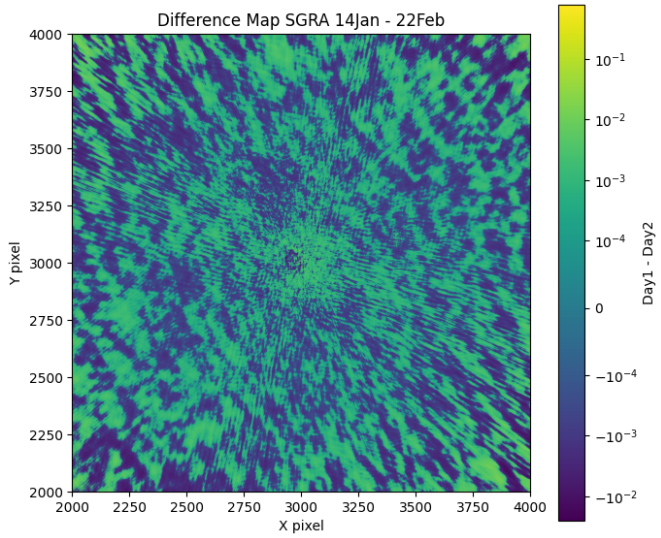

Figure 3.3.2: Difference map for the epoch pair 14 Jan – 22 Feb. Colour scale as in Figure 3.3.2.

14 Jan – 01 Apr

Figure 3.3.2 shows the 14 Jan – 01 Apr difference map. The field is broadly green-positive with a relatively uniform radial artefact pattern. The residual texture is smoother and more regular than maps involving the 22 Feb epoch, reflecting more comparable imaging conditions between these two epochs.

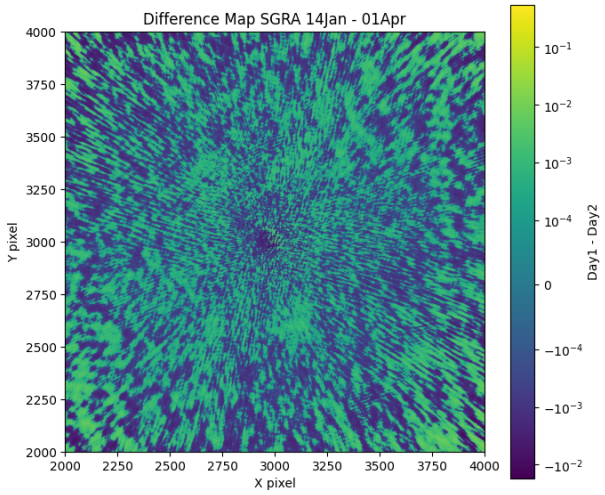

Figure 3.3.2: Difference map for the epoch pair 14 Jan – 01 Apr. Colour scale as in Figure 3.3.2.

22 Feb – 01 Apr

Figure 3.3.2 shows the 22 Feb – 01 Apr difference map. This map is morphologically distinct from all other pairs. The radial spoke pattern is less dominant, and large roughly circular blue-purple patches fill the outer regions of the field. This coarser incoherent structure is consistent with the elevated rms noise of the 22 Feb

epoch ($\sigma_{\mathrm{Feb}} = 1.872$ mJy beam^{-1}), the highest among all five epochs, propagating into the difference map. The combined noise for this pair is $\sigma_{\mathrm{diff}} = \sqrt{\sigma_{\mathrm{Feb}}^2 + \sigma_{\mathrm{Apr}}^2} = \sqrt{(1.872)^2 + (1.197)^2} \approx 2.22$ mJy beam^{-1}, the largest of all ten pairs.

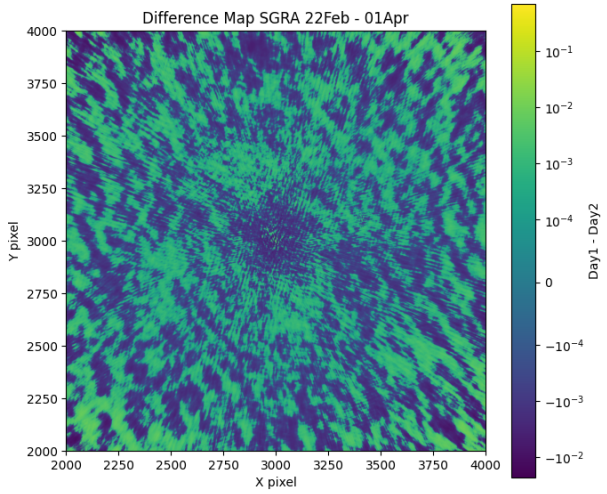

Figure 3.3.2: Difference map for the epoch pair 22 Feb − 01 Apr. Colour scale as in Figure 3.3.2.

3.6 Percentage Variation Maps

The percentage variation maps were derived directly from the difference maps constructed in Section 3.5. For each epoch pair (i, j), the percentage variation map is defined as

$$\mathcal{P}_{ij} = \frac{\mathcal{D}_{ij}}{\frac{1}{2}(I_i^{\mathrm{pb}} + I_j^{\mathrm{pb}})} \times 100\% = \frac{I_i^{\mathrm{pb}} - I_j^{\mathrm{pb}}}{\frac{1}{2}(I_i^{\mathrm{pb}} + I_j^{\mathrm{pb}})} \times 100\%, \tag{3.2}$$

where $\mathcal{D}_{ij} = I_i^{\mathrm{pb}} - I_j^{\mathrm{pb}}$ is the difference map and I_i^{pb}, I_j^{pb} are the primary-beam-corrected images of epochs i and j respectively. This normalisation by the mean of the two epoch fluxes at each pixel converts the absolute residuals of the difference maps into a dimensionless fractional measure of variability, independent of the absolute brightness at each location. Each map is displayed as a sky cutout in WCS coordinates, covering the RA range $17^{\mathrm{h}}44^{\mathrm{m}}00^{\mathrm{s}}$–$17^{\mathrm{h}}46^{\mathrm{m}}20^{\mathrm{s}}$ and Dec range -28 deg $50'$ to -29 deg $10'$, on a linear colour scale from 0 to 7‰, where yellow indicates high fractional variation and dark purple indicates low fractional variation. All ten maps share a common morphological structure: a dark (low percentage variation) central region centred on the Sgr A complex (Balick and Brown, 1974) near $(\alpha, \delta) \approx (17^{\mathrm{h}}45^{\mathrm{m}}40^{\mathrm{s}}, -29\,\mathrm{deg}\,00')$, surrounded by a yellow (high percentage variation) outer field. The dark central region arises because the Sgr A complex is bright in both epochs being compared, so the normalisation by the mean flux suppresses the fractional variation even where absolute flux differences exist. The yellow outer field corresponds to regions of low absolute flux where small absolute differences, including noise, produce large fractional values. The radial streak artefacts present in the difference maps are also visible in the percentage maps as fine radial structures extending from the central region into the outer field, arising from the same beam sidelobe mismatch described in Section 3.5 (Thompson, Moran, and Swenson

Jr., 2017). The key distinguishing feature across the ten maps is the spatial extent and morphology of the central dark region.

26 Oct / 14 Nov

Figure 3.3.2 shows the 26 Oct/14 Nov percentage variation map. The central dark region is relatively compact, confined primarily within $\sim 5'$ of the Sgr A complex near $\delta \approx -29\,\mathrm{deg}\,00'$. The transition from the dark central zone to the yellow outer field is relatively sharp, and fine radial streak structure is visible throughout the outer field.

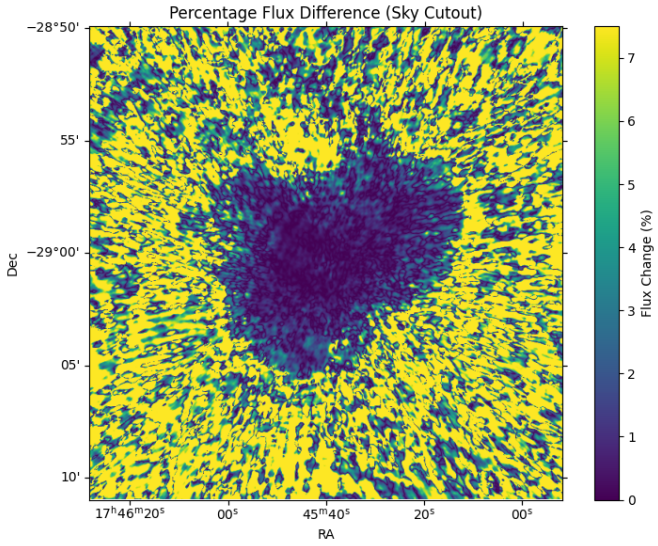

Figure 3.3.2: Percentage flux variation map for the epoch pair 26 Oct/14 Nov. The colour scale runs linearly from 0% (dark purple, low fractional variation) to 7% (yellow, high fractional variation).

26 Oct / 14 Jan

Figure 3.3.2 shows the 26 Oct/14 Jan percentage variation map. The central dark region is slightly larger in spatial extent compared to the 26 Oct/14 Nov map, with the low-variation zone extending further from the Sgr A complex. The outer field retains a similar fine radial streak structure.

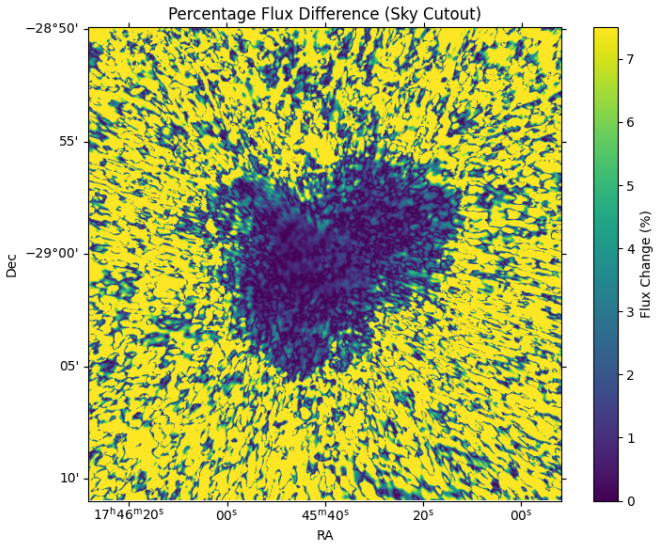

Figure 3.3.2: Percentage flux variation map for the epoch pair 26 Oct/14 Jan. Colour scale as in Figure 3.3.2.

26 Oct / 22 Feb

Figure 3.3.2 shows the 26 Oct/22 Feb percentage variation map. This map shows the most spatially extended central dark region among all pairs involving the 26 Oct epoch, with the low-variation zone spreading noticeably further south past $\delta \approx -29$ deg 05′. The dark region occupies a larger fraction of the total map area compared to the 26 Oct/14 Nov and 26 Oct/14 Jan pairs.

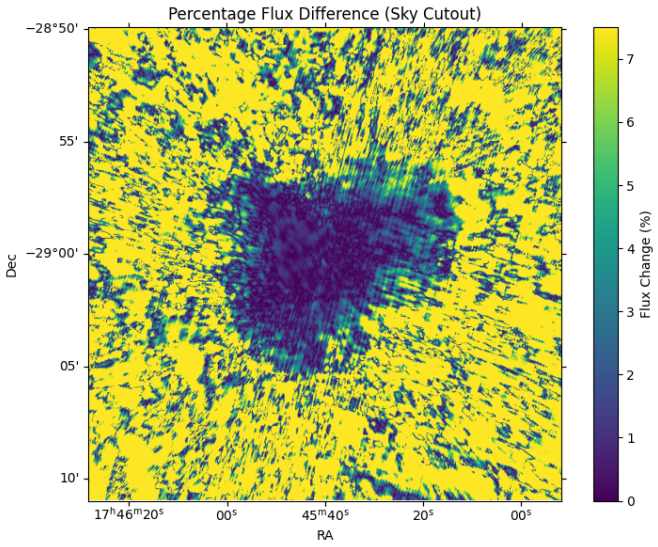

Figure 3.3.2: Percentage flux variation map for the epoch pair 26 Oct/22 Feb. Colour scale as in Figure 3.3.2.

26 Oct / 01 Apr

Figure 3.3.2 shows the 26 Oct/01 Apr percentage variation map. The central dark region extends clearly past $\delta \approx -29$ deg 05′ and the outer yellow field shows a coarser blob-like structure compared to the 26 Oct/14 Nov map, with less prominent fine radial streaking.

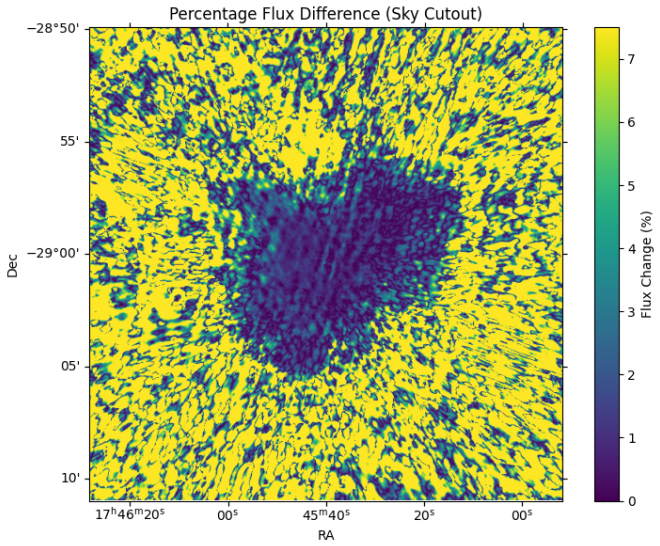

Figure 3.3.2: Percentage flux variation map for the epoch pair 26 Oct/01 Apr. Colour scale as in Figure 3.3.2.

14 Nov / 14 Jan

Figure 3.3.2 shows the 14 Nov/14 Jan percentage variation map. The central dark region is comparable in spatial extent to the 26 Oct/14 Nov map, with a relatively compact low-variation zone and fine radial streak structure in the outer yellow field.

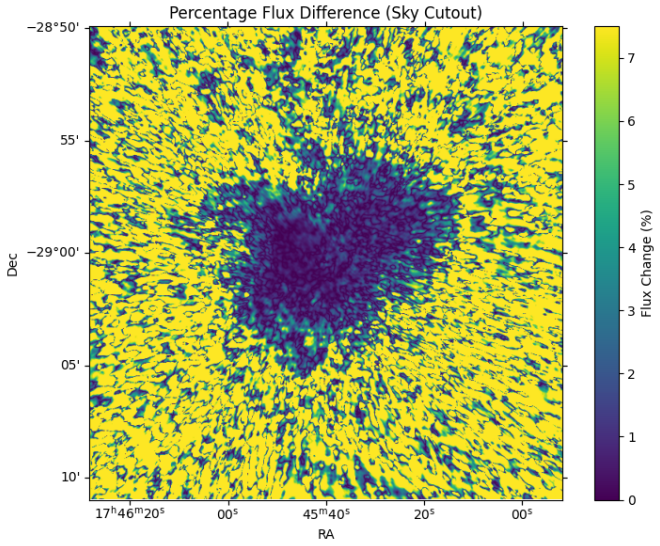

Figure 3.3.2: Percentage flux variation map for the epoch pair 14 Nov/14 Jan. Colour scale as in Figure 3.3.2.

14 Nov / 22 Feb

Figure 3.3.2 shows the 14 Nov/22 Feb percentage variation map. The central dark region is larger than in the 14 Nov/14 Jan map, with the low-variation zone extending further from the Sgr A complex. The boundary between the dark central region and the yellow outer field is more diffuse compared to the 14 Nov/14 Jan map, with teal-coloured intermediate-variation patches visible at the periphery of the central zone.

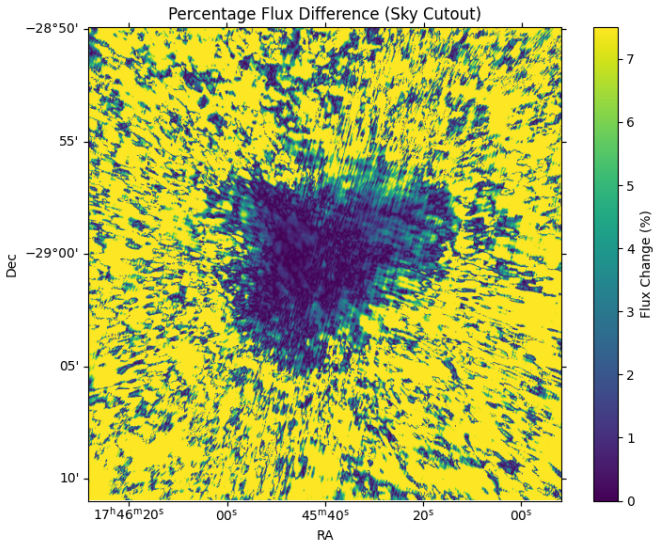

Figure 3.3.2: Percentage flux variation map for the epoch pair 14 Nov/22 Feb. Colour scale as in Figure 3.3.2.

14 Nov / 01 Apr

Figure 3.3.2 shows the 14 Nov/01 Apr percentage variation map. This map shows the largest central dark region among all pairs involving the 14 Nov epoch, extending clearly past $\delta \approx -29\,\mathrm{deg}\,05'$. The outer yellow field shows a coarser patch structure compared to the 14 Nov/14 Jan map.

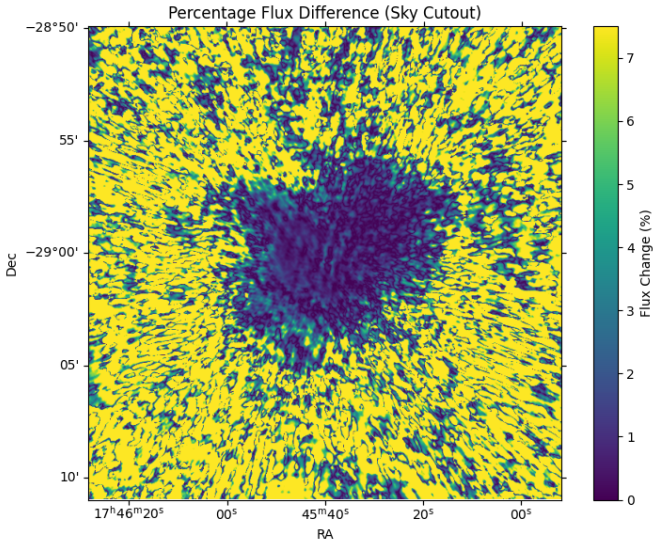

Figure 3.3.2: Percentage flux variation map for the epoch pair 14 Nov/01 Apr. Colour scale as in Figure 3.3.2.

14 Jan / 22 Feb

Figure 3.3.2 shows the 14 Jan/22 Feb percentage variation map. The central dark region is large and spatially extended, spreading well past $\delta \approx -29\,\mathrm{deg}\,00'$ toward $-29\,\mathrm{deg}\,05'$. The boundary of the dark region is irregular, with teal-coloured intermediate-variation patches visible at the periphery of the central zone.

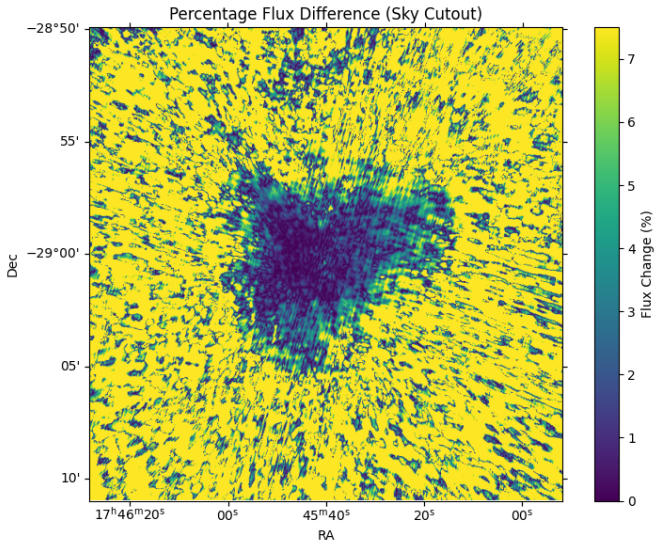

Figure 3.3.2: Percentage flux variation map for the epoch pair 14 Jan/22 Feb. Colour scale as in Figure 3.3.2.

14 Jan / 01 Apr

Figure 3.3.2 shows the 14 Jan/01 Apr percentage variation map. The central dark region is large and comparable in spatial extent to the 14 Jan/22 Feb map, with the low-variation zone extending similarly past $\delta \approx -29\,\mathrm{deg}\,00'$. The outer yellow field shows fine radial streak structure similar to that seen in the 14 Jan/22 Feb map.

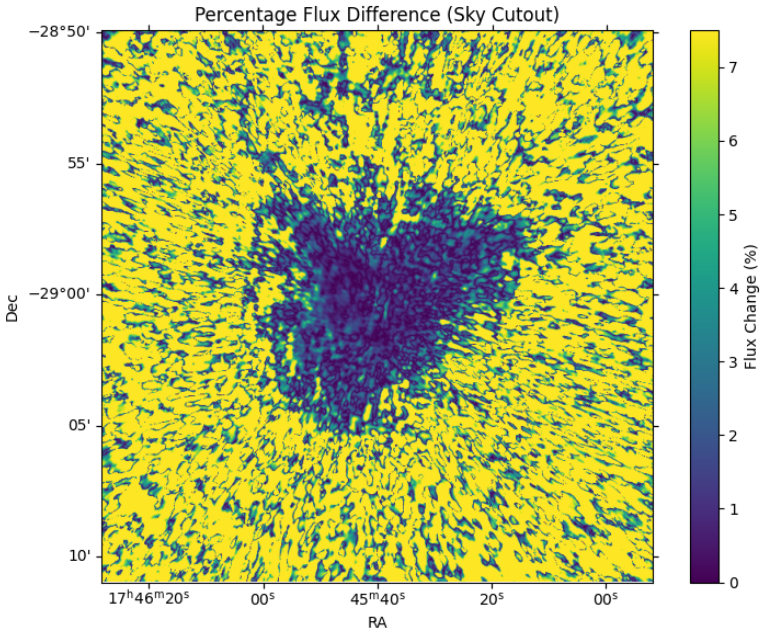

Figure 3.3.2: Percentage flux variation map for the epoch pair 14 Jan/01 Apr. Colour scale as in Figure 3.3.2.

22 Feb / 01 Apr

Figure 3.3.2 shows the 22 Feb/01 Apr percentage variation map. This map is morphologically distinct from all other pairs. The central dark region is the most compact among all ten maps, confined closely around the Sgr A complex near $\delta \approx -29\,\mathrm{deg}\,00'$, and the outer yellow field is the most spatially extensive of all ten pairs. The outer field shows a coarser blob-like texture rather than the fine radial streak structure seen in pairs not involving the 22 Feb epoch, consistent with the elevated rms noise of the 22 Feb observation ($\sigma_{\mathrm{Feb}} = 1.872$ mJy beam^{-1}) propagating into the percentage map through its contribution to both the numerator and denominator of $\mathcal{P}_{ij}$.

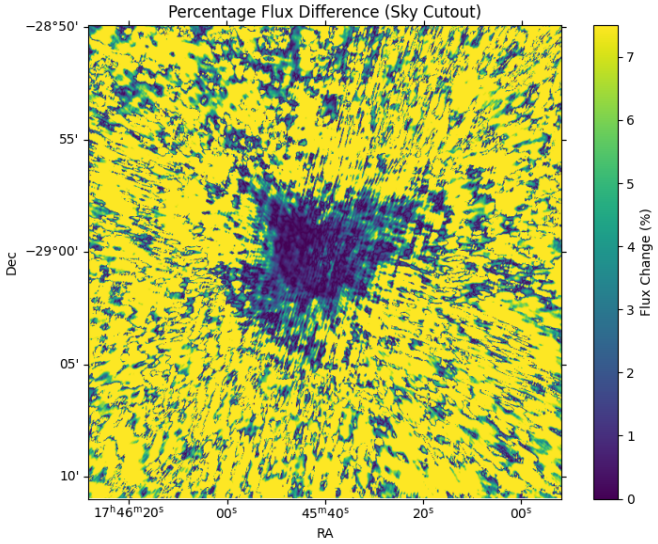

Figure 3.3.2: Percentage flux variation map for the epoch pair 22 Feb/01 Apr. Colour scale as in Figure 3.3.2.

3.7 In-Band Spectral Index Maps of Some of the filaments near GC

In-band spectral index maps were produced for each of the six identified regions across all five epochs using the WSCLEAN multi-frequency synthesis output (Offringa and Smirnov, 2017). The spectral index α is defined through $S \propto \nu^{\alpha}$ (Condon and Ransom, 2016), where S is the flux density and ν is the frequency, and is computed pixel-by-pixel from the in-band spectral information fitted during the cleaning process. A significance mask (ds9mask) was applied to retain only pixels above the detection threshold, suppressing noise-dominated pixels outside the detected emission. Each map is displayed as a WCS sky cutout centred on the respective region. Note that G359.78+0.17 is not recovered above the mask threshold in the 14 Jan epoch and is therefore absent for that epoch.

3.7.1 G359.78+0.17

G359.78+0.17 is a curved arc-like structure centred near $\delta \approx -29\,\mathrm{deg}\,02'$ (Heywood et al., 2022), detected in four of the five epochs: 26 Oct, 14 Nov, 22 Feb, and 01 Apr. This region is consistent with emission associated with the Galactic Centre Radio Arc filamentary complex (Yusef-Zadeh, M. Morris, and Chance, 1984; Lang, M. Morris, and Echevarria, 1999)

In the 26 Oct epoch (Figure 3.4.33.4.3.1), α ranges from 0 to 0.04, with $\alpha_{\rm peak}$ = 0.035, $\langle\alpha\rangle$ = 0.0098, and an integrated flux of 1.332 Jy.

In the 14 Nov epoch (Figure 3.4.33.4.3.2), α ranges from 0 to 0.030, with $\alpha_{\rm peak}$ = 0.026, $\langle\alpha\rangle$ = 0.009, and an integrated flux of 1.433 Jy.

In the 22 Feb epoch (Figure 3.4.33.4.3.3), α ranges from −0.010 to 0.025, with $\alpha_{\rm peak}$ = 0.027, $\langle\alpha\rangle$ = 0.0024, and an integrated flux of 0.927 Jy, the lowest among the four epochs in which G359.78+0.17 is detected. Negative α values appear toward the edges of the arc.

In the 01 Apr epoch (Figure 3.4.33.4.3.4), α ranges from 0 to 0.04, with $\alpha_{\rm peak}$ = 0.032, $\langle\alpha\rangle$ = 0.0052, and an integrated flux of 1.749 Jy, the highest among all four epochs in which G359.78+0.17 is detected.

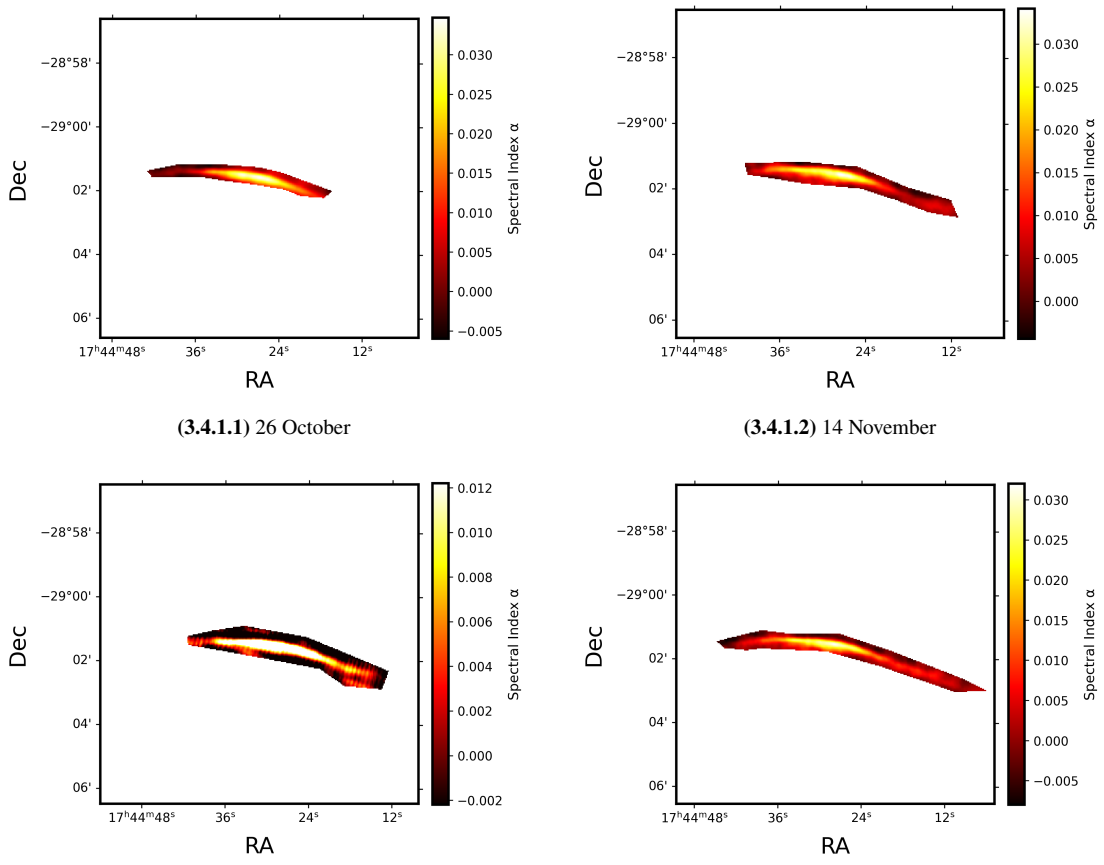

(3.4.1.1) 26 October

(3.4.1.2) 14 November

(3.4.1.3) 22 February

(3.4.1.4) 01 April

Figure 3.4.1: In-band spectral index maps of G359.78+0.17 for all four observing epochs. The colour scale represents the spectral index α, where $S_\nu \propto \nu^\alpha$.

3.7.2 G359.55+0.18

G359.55+0.18 is an elongated filamentary structure centred near $\delta \approx -29\,\mathrm{deg}\,14'$, detected in all five epochs (Heywood et al., 2022). The filamentary morphology is consistent with a non-thermal radio filament (Yusef-Zadeh, M. Morris, and Chance, 1984; Heywood et al., 2022).

In the 26 Oct epoch (Figure 3.4.23.4.2.1), α ranges from −0.0053 to 0.011, with $\alpha_{\rm peak}$ = 0.011, $\langle\alpha\rangle$ = 0.0009, and an integrated flux of 0.281 Jy.

In the 14 Nov epoch (Figure 3.4.23.4.2.2), α ranges from -0.004 to 0.010, with $\alpha_{\rm peak} = 0.009$, $\langle\alpha\rangle = 0.002$, and an integrated flux of 0.224 Jy.

In the 14 Jan epoch (Figure 3.4.23.4.2.3), α ranges from -0.004 to 0.008, with $\alpha_{\rm peak} = 0.008$, $\langle\alpha\rangle = 0.0028$, and an integrated flux of 0.395 Jy.

In the 22 Feb epoch (Figure 3.4.23.4.2.4), α ranges from -0.010 to 0.025, with $\alpha_{\rm peak} = 0.012$, $\langle\alpha\rangle = 0.0014$, and an integrated flux of 0.476 Jy. The map shows alternating yellow-red striping along the filament, consistent with noise artefacts in the spectral index fitting at the elevated rms of the 22 Feb epoch.

In the 01 Apr epoch (Figure 3.4.23.4.2.5), α ranges from -0.002 to 0.012, with $\alpha_{\rm peak} = 0.013$, $\langle\alpha\rangle = 0.0026$, and an integrated flux of 0.941 Jy, the highest among all five epochs for this region.

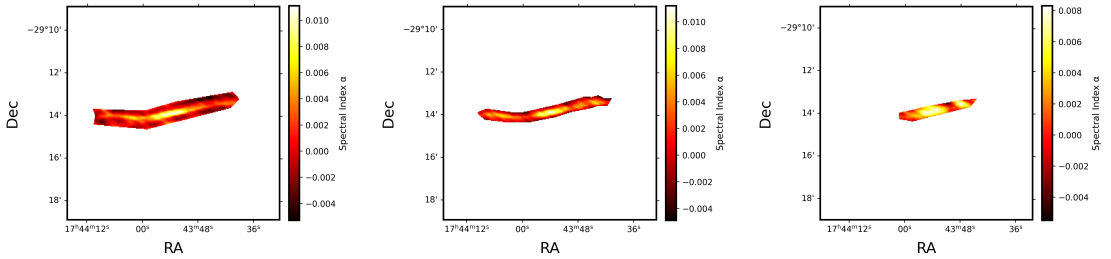

(3.4.2.1) 26 October **(3.4.2.2)** 14 November **(3.4.2.3)** 14 January

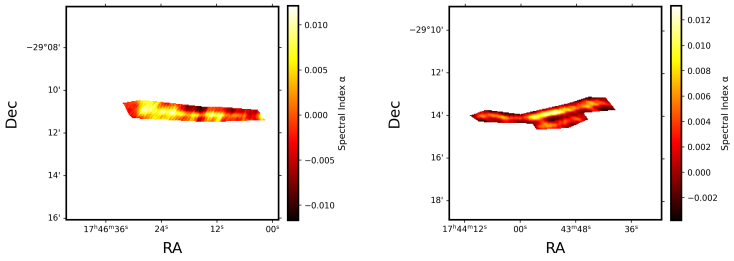

(3.4.2.4) 22 February **(3.4.2.5)** 01 April

Figure 3.4.2: In-band spectral index maps of G359.55+0.18 for all five observing epochs. The colour scale represents the spectral index α, where $S_\nu \propto \nu^\alpha$.

3.7.3 G359.83-0.28

G359.83-0.28 is a thin linear filament centred near $\delta \approx -29\,\mathrm{deg}\,11'$ (Heywood et al., 2022), detected in all five epochs. It is the most spatially compact of the six regions, consistent with a narrow non-thermal filament (Yusef-Zadeh, M. Morris, and Chance, 1984).

In the 26 Oct epoch (Figure **??**), α ranges from -0.0065 to 0.010, with $\alpha_{\rm peak} = 0.010$, $\langle\alpha\rangle = 0.0023$, and an integrated flux of 0.215 Jy.

In the 14 Nov epoch (Figure **??**), α ranges from -0.002 to 0.008, with $\alpha_{\rm peak} = 0.005$, $\langle\alpha\rangle = 0.0034$, and an integrated flux of 0.300 Jy.

In the 14 Jan epoch (Figure **??**), α ranges from -0.002 to 0.008, with $\alpha_{\rm peak} = 0.008$, $\langle\alpha\rangle = 0.0035$, and an integrated flux of 0.343 Jy.

In the 22 Feb epoch (Figure **??**), α ranges from -0.010 to 0.025, with $\alpha_{\rm peak} = 0.012$, $\langle\alpha\rangle = 0.0014$, and an integrated flux of 0.476 Jy. As noted previously, the 22 Feb statistics for G359.83-0.28 are identical to those of G359.55+0.18 in that epoch, which is flagged as a potential region-definition issue for that observation.

In the 01 Apr epoch (Figure **??**), α ranges from −0.005 to 0.0125, with $\alpha_{\rm peak}$ = 0.013, $\langle\alpha\rangle$ = 0.0016, and an integrated flux of 0.298 Jy.

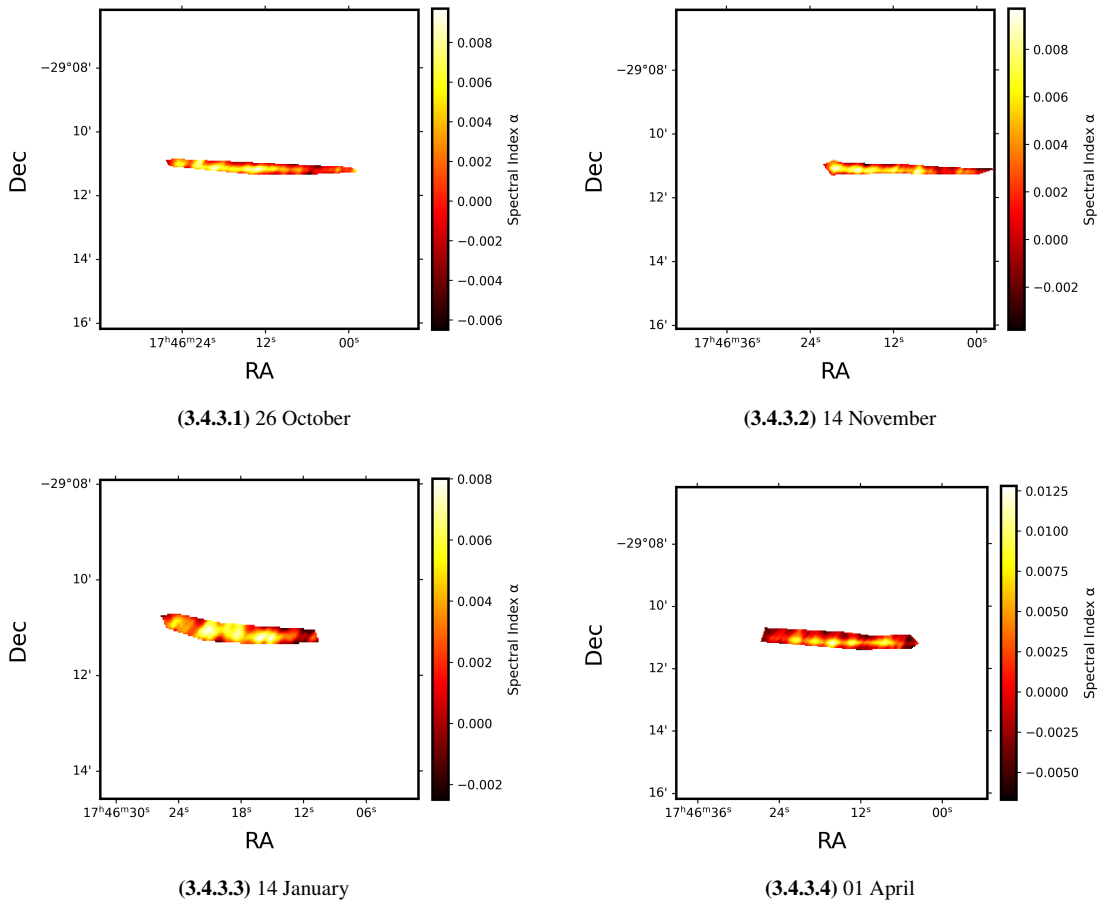

(3.4.3.1) 26 October

(3.4.3.2) 14 November

(3.4.3.3) 14 January

(3.4.3.4) 01 April

Figure 3.4.3: In-band spectral index maps of G359.83−0.28 for all five observing epochs. The colour scale represents the spectral index α, where $S_\nu \propto \nu^\alpha$.

3.7.4 G359.83-0.28

G0.08+0.15 is a diagonal filamentary structure located north of Sgr A (Heywood et al., 2022), spanning the Dec range −28 deg 44′ to −28 deg 55′, and detected in all five epochs. The structure shows significant internal spectral index variation in all epochs, consistent with the behaviour reported for Radio Arc filaments (Yusef-Zadeh, M. Morris, and Chance, 1984; Lang, M. Morris, and Echevarria, 1999; Heywood et al., 2022).

In the 26 Oct epoch (Figure 3.4.43.4.4.1), α ranges from −0.0081 to 0.030, with $\alpha_{\rm peak}$ = 0.030, $\langle\alpha\rangle$ = 0.0033, and an integrated flux of 1.035 Jy.

In the 14 Nov epoch (Figure 3.4.43.4.4.2), α ranges from −0.005 to 0.020, with $\alpha_{\rm peak}$ = 0.020, $\langle\alpha\rangle$ = 0.0039, and an integrated flux of 4.423 Jy.

In the 14 Jan epoch (Figure 3.4.43.4.4.3), α ranges from −0.005 to 0.015, with $\alpha_{\rm peak}$ = 0.019, $\langle\alpha\rangle$ = 0.0052, and an integrated flux of 3.049 Jy.

In the 22 Feb epoch (Figure 3.4.43.4.4.4), α ranges from −0.005 to 0.020, with $\alpha_{\rm peak}$ = 0.022, $\langle\alpha\rangle$ = 0.0042, and an integrated flux of 2.511 Jy.

In the 01 Apr epoch (Figure 3.4.43.4.4.5), α ranges from −0.010 to 0.020, with $\alpha_{\rm peak}$ = 0.021, $\langle\alpha\rangle$ = 0.0022, and an integrated flux of 3.933 Jy.

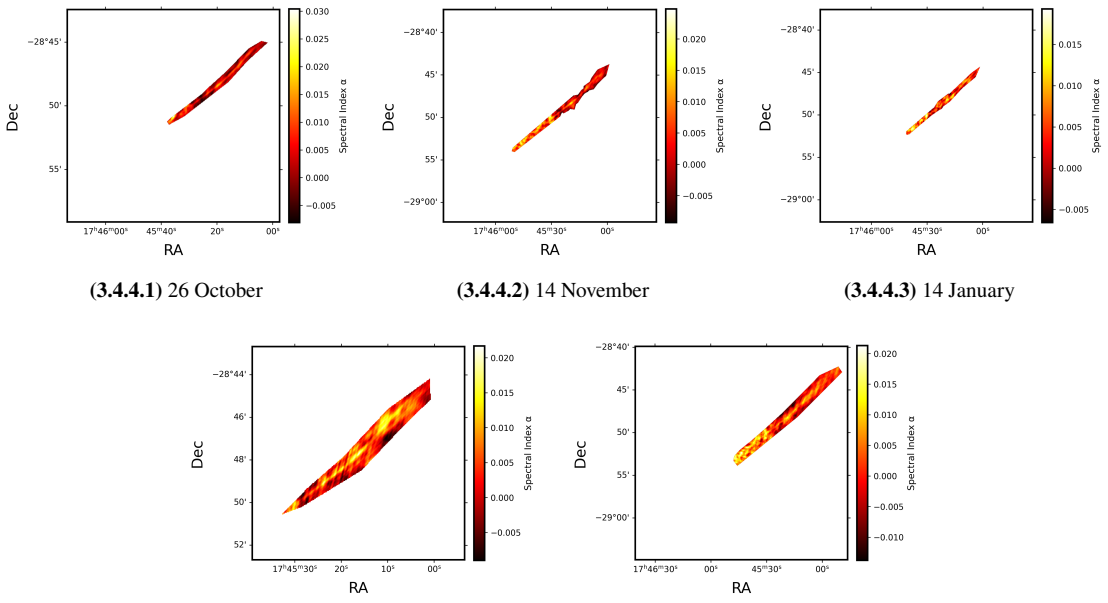

(3.4.4.1) 26 October **(3.4.4.2)** 14 November **(3.4.4.3)** 14 January

(3.4.4.4) 22 February **(3.4.4.5)** 01 April

Figure 3.4.4: In-band spectral index maps of G0.08+0.15 for all five observing epochs. The colour scale represents the spectral index α, where $S_\nu \propto \nu^\alpha$.

3.7.5 Radio Arc

Radio Arc is the largest region in the analysis, comprising a broad diffuse emission complex together with an arc-like filamentary component, located in the RA range $17^{\rm h}45^{\rm m}30^{\rm s}$–$17^{\rm h}47^{\rm m}00^{\rm s}$ and Dec range $-28\,\mathrm{deg}\,40'$ to $-29\,\mathrm{deg}\,00'$, and detected in all five epochs (Yusef-Zadeh, M. Morris, and Chance, 1984; M. Morris and Serabyn, 1996; Heywood et al., 2022). The final masked spectral index maps are used for the analysis.

In the 26 Oct epoch (Figure 3.4.53.4.5.1), α ranges from -0.012 to 0.024, with $\alpha_{\rm peak} = 0.024$, $\langle\alpha\rangle = 0.0054$, and an integrated flux of 16.516 Jy. A localised region of elevated α is visible at the southern boundary of the diffuse component.

In the 14 Nov epoch (Figure 3.4.53.4.5.2), α ranges from 0 to 0.020, with $\alpha_{\rm peak} = 0.022$, $\langle\alpha\rangle = 0.0034$, and an integrated flux of 15.884 Jy.

In the 14 Jan epoch (Figure 3.4.53.4.5.3), α ranges from 0 to 0.020, with $\alpha_{\rm peak} = 0.022$, $\langle\alpha\rangle = 0.0038$, and an integrated flux of 17.214 Jy.

In the 22 Feb epoch (Figure 3.4.53.4.5.4), α ranges from 0 to 0.150, with $\alpha_{\rm peak} = 0.027$, $\langle\alpha\rangle = 0.0057$, and an integrated flux of 24.362 Jy, the highest of all five epochs for this region. The colour scale extends to 0.15, substantially higher than in the other epochs, with a prominent localised spot of $\alpha \gtrsim 0.10$ visible at the southern boundary of the diffuse component at the same position as the elevated feature seen in the 26 Oct map.

In the 01 Apr epoch (Figure 3.4.53.4.5.5), α ranges from -0.010 to 0.020, with $\alpha_{\rm peak} = 0.020$, $\langle\alpha\rangle = 0.0034$, and an integrated flux of 16.358 Jy.

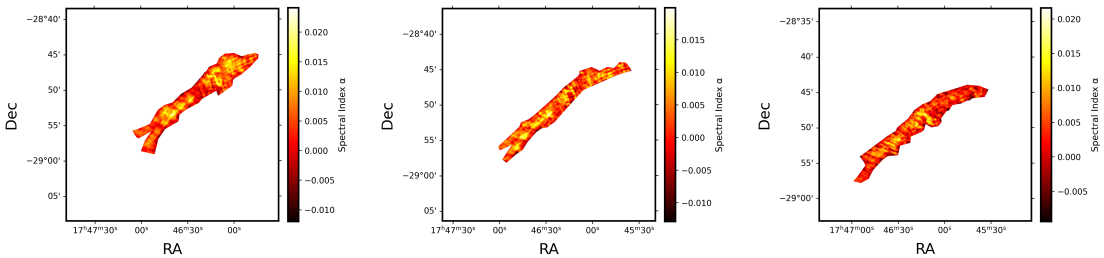

(3.4.5.1) 26 October **(3.4.5.2)** 14 November **(3.4.5.3)** 14 January

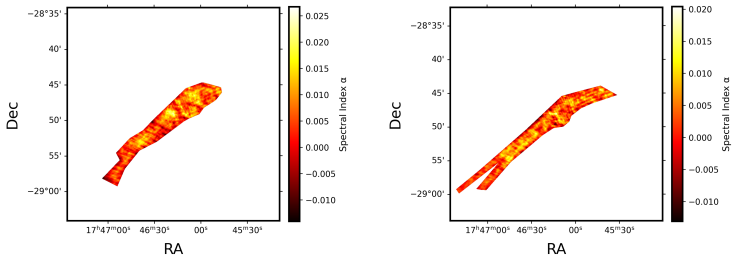

(3.4.5.4) 22 February **(3.4.5.5)** 01 April

Figure 3.4.5: In-band spectral index maps of the Radio Arc for all five observing epochs. The colour scale represents the spectral index α, where $S_\nu \propto \nu^\alpha$.

3.7.6 G359.45-0.04

G359.45-0.04 is an elongated filament located to the south-east of Sgr A (Heywood et al., 2022), centred near $\delta \approx -29$ deg 26′, and detected in all five epochs. Its elongated morphology is consistent with the class of non-thermal radio filaments identified in the Galactic Centre (Yusef-Zadeh, M. Morris, and Chance, 1984; Heywood et al., 2022).

In the 26 Oct epoch (Figure 3.4.63.4.6.1), α ranges from −0.000193 to 0.016, with $\alpha_{\rm peak} = 0.016$, $\langle\alpha\rangle = 0.0157$, and an integrated flux of 0.989 Jy.

In the 14 Nov epoch (Figure 3.4.63.4.6.2), α ranges from −0.002 to 0.012, with $\alpha_{\rm peak} = 0.010$, $\langle\alpha\rangle = 0.0041$, and an integrated flux of 0.419 Jy.

In the 14 Jan epoch (Figure 3.4.63.4.6.3), α ranges from −0.010 to 0.020, with $\alpha_{\rm peak} = 0.008$, $\langle\alpha\rangle = 0.0036$, and an integrated flux of 0.227 Jy, the lowest among all five epochs for this region.

In the 22 Feb epoch (Figure 3.4.63.4.6.4), α ranges from −0.006 to 0.010, with $\alpha_{\rm peak} = 0.010$, $\langle\alpha\rangle = 0.0016$, and an integrated flux of 0.969 Jy.

In the 01 Apr epoch (Figure 3.4.63.4.6.5), α ranges from −0.002 to 0.015, with $\alpha_{\rm peak} = 0.017$, $\langle\alpha\rangle = 0.0045$, and an integrated flux of 1.099 Jy, the highest among all five epochs for this region.

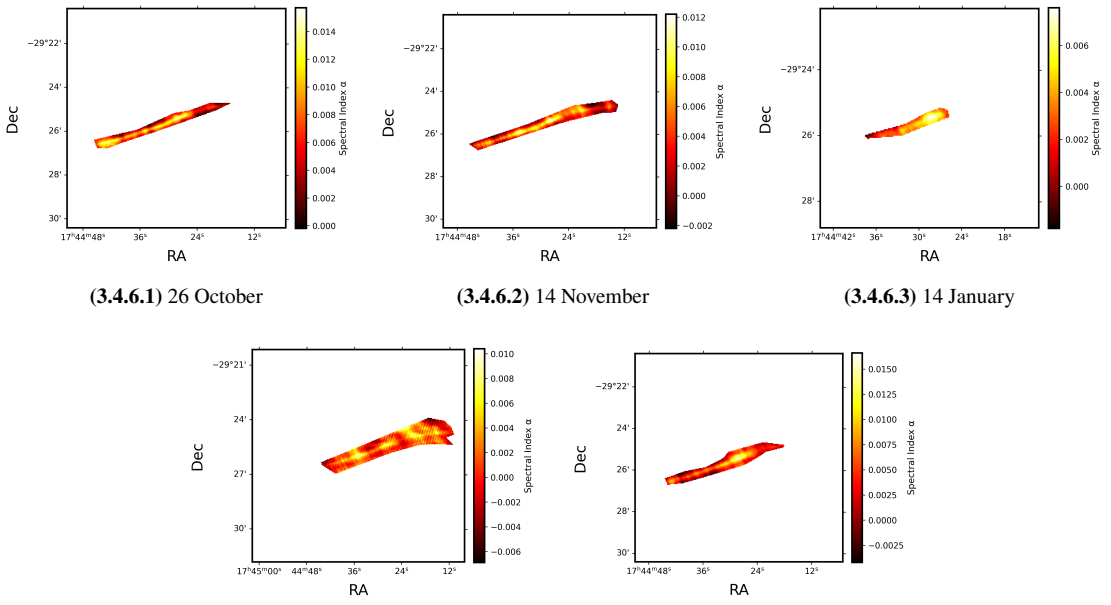

(3.4.6.1) 26 October **(3.4.6.2)** 14 November **(3.4.6.3)** 14 January

(3.4.6.4) 22 February **(3.4.6.5)** 01 April

Figure 3.4.6: In-band spectral index maps of G359.45−0.04 for all five observing epochs. The colour scale represents the spectral index α, where $S_\nu \propto \nu^\alpha$.

3.8 Physical Lengths of Identified Filaments

The angular extents of the six identified filamentary regions were measured from the in-band spectral index maps across all five observing epochs. The physical length L of each filament was derived from the measured angular extent θ (in arcseconds) using the small-angle approximation

$$L = d \cdot \frac{\theta}{206265} pc, \tag{3.3}$$

where $d = 8.2$ kpc is the adopted distance to the Galactic Centre (GRAVITY Collaboration et al., 2019). At this distance, 1 arcsecond corresponds to a physical scale of ≈ 0.03965 pc. The derived physical lengths for all five epochs are listed in Table 3.2.

Table 3.2: Measured angular extents (θ, in arcseconds) and derived physical lengths (L, in pc) of the six identified filamentary regions for each of the five observing epochs. $\theta = 2 \times \theta_{\rm half}$ as measured from the spectral index maps.

	26 Oct		**14 Nov**		**14 Jan**		**22 Feb**		**01 Apr**	
Region	θ (asec)	L (pc)	θ (asec)	L (pc)	θ (asec)	L (pc)	θ (asec)	L (pc)	θ (asec)	L (pc)
G359.78+0.17	450.39	17.86	431.70	17.12	402.52	15.96	398.14	15.79	431.70	17.12
G359.55+0.18	434.00	17.21	388.66	15.65	358.39	14.21	429.94	17.05	413.47	16.39
G359.83-0.28	273.99	10.86	345.40	13.69	206.48	8.19	335.80	13.31	321.23	12.74
G0.08+0.15	940.18	37.28	949.09	37.63	955.64	37.89	950.99	37.70	617.63	24.49
Radio Arc	1347.19	53.41	1226.24	48.62	1425.81	56.53	1350.26	53.53	1425.81	56.53
G359.45-0.04	488.55	19.37	469.40	18.61	251.00	9.95	486.54	19.29	513.57	20.36

The physical lengths of the filaments range from approximately 8.2 pc (G359.83-0.28, 14 Jan epoch) to $\sim$ 56.5 pc (Radio Arc, 14 Jan and 01 Apr epochs), consistent with

the known size range of non-thermal filaments in the Galactic Centre, which typically span 10–40 pc in length (Yusef-Zadeh, M. Morris, and Chance, 1984; Heywood et al., 2022). Radio Arc, the largest region in the analysis, shows the greatest physical extent across all epochs, reaching up to ∼ 56.5 pc. Regions 2, 3, and 7 are more compact, with lengths generally in the range 8–21 pc. The lengths are broadly consistent across the five epochs for most regions. A notable exception is G0.08+0.15, which shows a significantly reduced length in the 01 April epoch (∼ 24.5 pc) compared to the other four epochs (∼ 37–38 pc), and G359.45-0.04, which shows a substantially shorter length in the 14 January epoch (∼ 10 pc) compared to the other epochs (∼ 18–20 pc), likely reflecting differences in surface brightness sensitivity between epochs at those positions.

3.9 Multi-wavelength Comparison with Infrared Data

The uGMRT Band 4 radio continuum maps of the Galactic Centre region were compared with infrared data from 2MASS and WISE to investigate the multi-wavelength properties of the detected structures. The infrared emission is overlaid as contour maps on the radio images to examine spatial correlations between thermal and non-thermal components.

The central region is dominated by the bright Sgr A complex, which is clearly detected in both radio and infrared wavelengths. The strong spatial coincidence between radio emission and infrared contours indicates the presence of dense stellar populations and ionised gas in the Galactic Centre. However, the radio emission appears more extended compared to the infrared distribution, suggesting the presence of diffuse synchrotron emission in addition to thermal components.

Several filamentary structures are observed surrounding the central source. These structures are prominently visible in the radio maps and are partially traced by the infrared contours. The incomplete correspondence between radio and infrared emission suggests that many of these filaments are dominated by non-thermal synchrotron processes rather than thermal dust emission, supporting their identification as non-thermal filaments associated with strong magnetic fields in the Galactic Centre.

The infrared contours exhibit a clumpy and fragmented morphology, reflecting the distribution of dust and stellar sources, whereas the radio emission shows both compact and diffuse components. This difference highlights the distinct physical origins of emission in the two wavelength regimes.

A comparison across multiple observing epochs shows that the overall morphology of both radio and infrared structures remains consistent. While slight variations in radio brightness are observed, these are attributed to imaging systematics such as uv-coverage differences and calibration uncertainties rather than intrinsic variability of the source.

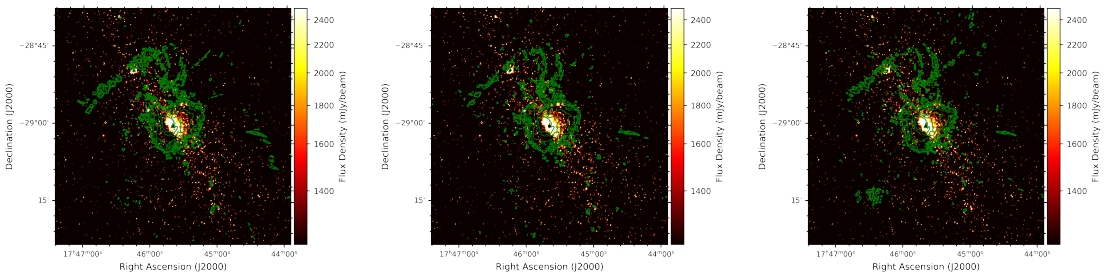

(3.6.1) 26 October **(3.6.2)** 14 November **(3.6.3)** 14 January

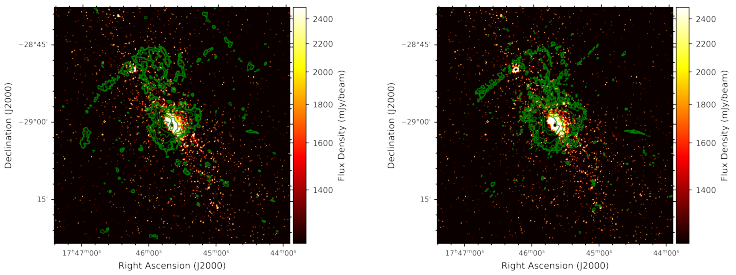

(3.6.4) 22 February **(3.6.5)** 01 April

Figure 3.6: Multi-epoch overlay of uGMRT Band 4 radio continuum emission with infrared contours (WISE) for the Galactic Centre region. The colour scale represents radio flux density (mJy beam^{-1}), while green contours indicate infrared emission. The central bright source corresponds to the Sgr A complex. Extended diffuse emission and filamentary structures are visible, with partial correspondence to infrared features, indicating a mixture of thermal and non-thermal emission processes.

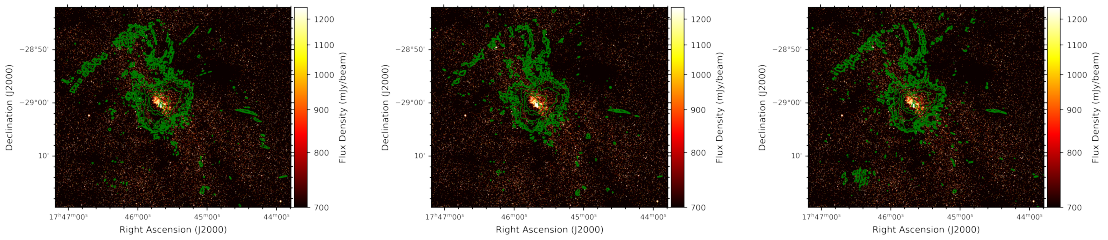

(3.7.1) 26 October **(3.7.2)** 14 November **(3.7.3)** 14 January

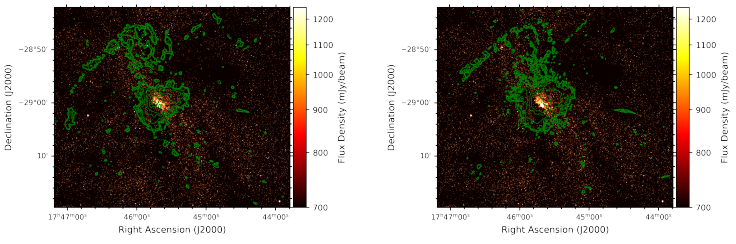

(3.7.4) 22 February **(3.7.5)** 01 April

Figure 3.7: Multi-epoch overlay of uGMRT Band 4 radio continuum emission with 2MASS infrared contours for the Galactic Centre region. The infrared emission traces stellar populations and dust, while the radio emission reveals both compact and diffuse structures. The comparison highlights differences between thermal infrared emission and non-thermal radio emission, particularly in the filamentary regions.

3.10 Summary

This thesis presented a detailed radio continuum study of the Galactic Centre region using multi-epoch uGMRT Band 4 (550–850 MHz) observations across five epochs

from October 2013 to April 2014. High-sensitivity radio continuum maps were produced using wide-field multi-scale imaging with WSClean, revealing a morphologically complex field dominated by the Sgr A complex, surrounded by diffuse emission and elongated filamentary structures. Six filamentary regions — G359.78+0.17, G359.55+0.18, G359.83-0.28, G0.08+0.15, the Radio Arc, and G359.45-0.04 — were identified and characterized with physical lengths ranging from approximately 8 pc to 57 pc, consistent with the known population of non-thermal filaments in the Galactic Centre.

Multi-epoch difference maps and percentage variation maps constructed from primary beam corrected images show epoch-to-epoch flux variations of roughly 15%, attributed primarily to imaging systematics such as synthesised beam size differences, uv-coverage variations, and residual calibration offsets rather than genuine astrophysical variability. At Band 4 frequencies, Sgr A* is heavily scatter-broadened by the intervening ionised medium, further limiting variability constraints.

In-band spectral index mapping across all six regions yielded consistently near-flat values with $\langle\alpha\rangle \approx 0.001$–$0.016$ and peak values not exceeding $\alpha \approx 0.04$. While these are not inconsistent with non-thermal synchrotron emission, the narrow in-band frequency coverage limits the measurement precision, and the flat spectral indices alone are insufficient to conclusively distinguish between thermal free–free and non-thermal synchrotron emission. A definitive classification of these filaments as non-thermal structures therefore cannot be established from the present results alone. Polarisation observations, combined with Faraday rotation measure synthesis and multi-frequency follow-up across uGMRT Band 3, Band 4, and Band 5, are identified as the critical next steps to firmly confirm the non-thermal nature of these candidate filamentary structures.

Chapter 4

Future Plans

4.1 Characterisation of the Detected Filaments

Six filamentary regions were identified and mapped for in-band spectral index. None of these are definitively classified in the thesis. Future work should include polarisation measurements to confirm synchrotron emission and probe magnetic field orientation, multi-wavelength counterpart searches (infrared, X-ray) to distinguish thermal from non-thermal origins, and Faraday rotation measure synthesis to probe the magnetised plasma along the line of sight.

4.2 Identifying New SNR Candidates

The thesis focuses primarily on the Sgr A complex region. A dedicated source extraction and morphological classification effort applied to the full $3.3^\circ \times 3.3^\circ$ field, combined with multi-wavelength overlays using existing infrared and X-ray surveys, could yield new SNR candidates by identifying shell-like structures lacking infrared counterparts.

4.3 Multi-frequency Follow-up

Combine Band 4 with uGMRT Band 3 (300–500 MHz) and Band 5 (1050–1450 MHz) to measure spectral index α across a wider frequency baseline. This would allow more definitive confirmation of the thermal or non-thermal nature of the candidate filamentary regions, since the narrow in-band α values recovered in this thesis are insufficient to conclusively classify structures as SNR candidates.

REFERENCES

Anderson, L. D. et al. (Jan. 2025). "Supernova remnant candidates discovered by the SARAO MeerKAT Galactic Plane Survey". In: 693, A247, A247. DOI: 10.1051/0004-6361/202451038. arXiv: 2409.16607 [astro-ph.GA].

Baganoff, F. K. et al. (2001). "Rapid X-ray flaring from the direction of the supermassive black hole at the Galactic Centre". In: *Nature* 413, pp. 45–48. DOI: 10.1038/35092510.

Balick, B. and R. L. Brown (1974). "Intense sub-arcsecond structure in the galactic center". In: *ApJ* 194, pp. 265–270. DOI: 10.1086/153242.

Beck, R. (2015). "Galactic and extragalactic magnetic fields". In: *Astronomy & Astrophysics Review* 24, p. 4. DOI: 10.1007/s00159-015-0084-4.

Bell, A. R. (1978). "The acceleration of cosmic rays in shock fronts". In: *MNRAS* 182, pp. 147–156. DOI: 10.1093/mnras/182.2.147.

Beuther, H. et al. (2016). "The HI/OH/Recombination line survey of the inner Milky Way (THOR): Survey overview and data release 1". In: *A&A* 595, A32. DOI: 10.1051/0004-6361/201629143.

Blasi, P. (2013). "The origin of galactic cosmic rays". In: *A&ARv* 21, p. 70. DOI: 10.1007/s00159-013-0070-7.

Bower, G. C. et al. (2006). "Detection of the Intrinsic Size of Sagittarius A* Through Closure Amplitude Imaging". In: *ApJ* 648, pp. L127–L130. DOI: 10.1086/507861.

— (2014). "The Angular Broadening of the Galactic Center Pulsar SGR J1745-29". In: *ApJ* 798, p. 120. DOI: 10.1088/0004-637X/798/2/120.

Bower, G. C., H. Falcke, et al. (2004). "Detection of the Intrinsic Size of Sagittarius A* Through Closure Amplitude Imaging". In: *Science* 304.5671, pp. 704–708. DOI: 10.1126/science.1094392.

Bower, G. C., S. Markoff, et al. (2015). "Radio and Millimeter Monitoring of Sgr A*: Spectrum, Variability, and Constraints on the G2 Encounter". In: *The Astrophysical Journal* 802.1, p. 69. DOI: 10.1088/0004-637X/802/1/69.

Chevalier, R. A. (1977). "The interaction of supernovae with the interstellar medium". In: *ARA&A* 15, pp. 175–196. DOI: 10.1146/annurev.aa.15.090177.001135.

Cioffi, D. F., C. F. McKee, and E. Bertschinger (1988). "Dynamics of radiative supernova remnants". In: *ApJ* 334, pp. 252–265. DOI: 10.1086/166834.

Ciurlo, Anna and Mark R. Morris (Mar. 2025). "Sagittarius A* – The Milky Way Supermassive Black Hole". In: *arXiv e-prints*, arXiv:2503.20081, arXiv:2503.20081. DOI: 10.48550/arXiv.2503.20081. arXiv: 2503.20081 [astro-ph.GA].

Condon, J. J., W. D. Cotton, et al. (1998). "The NRAO VLA Sky Survey". In: *AJ* 115, pp. 1693–1716. DOI: 10.1086/300337.

Condon, J. J. and S. M. Ransom (2016). *Essential Radio Astronomy*. Princeton University Press. URL: https://www.cv.nrao.edu/~sransom/web/xxx.html.

Cornwell, T. J. and P. N. Wilkinson (1981). "A new method for making maps with unstable radio interferometers". In: *MNRAS* 196, pp. 1067–1086.

Dokara, R., A. Brunthaler, et al. (2021). "A global view on star formation: The GLOSTAR Galactic plane survey. II. Supernova remnants in the first quadrant of the Milky Way". In: *A&A* 651, A86. DOI: 10.1051/0004-6361/202039873.

Dokara, R., Y. Gong, et al. (Mar. 2023). "A global view on star formation: The GLOSTAR Galactic plane survey. VII. Supernova remnants in the Galactic longitude range 28°

< l < 36°". In: 671, A145, A145. DOI: 10.1051/0004-6361/202245339. arXiv: 2211.13811 [astro-ph.GA].
Eatough, R. P. et al. (2013). "A strong magnetic field around the supermassive black hole at the centre of the Galaxy". In: *Nature* 501, pp. 391–394. DOI: 10.1038/nature12499.
Gaensler, B. M. and P. O. Slane (2006). "The Evolution and Structure of Pulsar Wind Nebulae". In: *ARA&A* 44, pp. 17–47. DOI: 10.1146/annurev.astro.44.051905.092528.
Genzel, R. et al. (2003). "Near-infrared flares from accreting gas around the supermassive black hole at the Galactic Centre". In: *Nature* 425, pp. 934–937. DOI: 10.1038/nature02065.
Ghez, A. M. et al. (2008). "Measuring Distance and Properties of the Milky Way's Central Supermassive Black Hole with Stellar Orbits". In: *The Astrophysical Journal* 689.2, pp. 1044–1062. DOI: 10.1086/592738.
Gillessen, S. et al. (2009). "Monitoring Stellar Orbits Around the Massive Black Hole in the Galactic Center". In: *The Astrophysical Journal* 692.2, pp. 1075–1109. DOI: 10.1088/0004-637X/692/2/1075.
Ginzburg, V. L. and S. I. Syrovatskii (1965). *The Origin of Cosmic Rays*. Pergamon Press.
GRAVITY Collaboration et al. (2019). "A geometric distance measurement to the Galactic Center black hole". In: *A&A* 625, p. L10. DOI: 10.1051/0004-6361/201935656.
Green, D. A. (2019). "A catalogue of 294 Galactic supernova remnants". In: *JApA* 40, p. 36. DOI: 10.1007/s12036-019-9601-6.
Gupta, Y. et al. (2017a). "The upgraded GMRT: opening new windows on the radio Universe". In: *CSci* 113, pp. 707–714.
— (2017b). "The upgraded GMRT: opening new windows on the radio Universe". In: *Current Science* 113, pp. 707–714.
Haarlem, M. P. van, M. W. Wise, A. W. Gunst, et al. (2013). "LOFAR: The LOw-Frequency ARray". In: *A&A* 556, A2. DOI: 10.1051/0004-6361/201220873.
Haslam, C. G. T. et al. (1982). "A 408 MHz all-sky continuum survey. II. The atlas of contour maps". In: *Astronomy & Astrophysics Supplement Series* 47, p. 1.
Heywood, I. et al. (2019). "Inflation of 430-parsec bipolar radio bubbles in the Galactic Centre by an energetic event". In: *Nature* 573, pp. 237–240. DOI: 10.1038/s41586-019-1532-5.
— (2022). "The 1.28 GHz MeerKAT Galactic Center Mosaic". In: *ApJ* 925, p. 165. DOI: 10.3847/1538-4357/ac449a.
Hillebrandt, W. and J. C. Niemeyer (2000). "Type Ia Supernova Explosion Models". In: *ARA&A* 38, pp. 191–230. DOI: 10.1146/annurev.astro.38.1.191.
Hou, L. G., J. L. Han, and W. B. Shi (May 2009). "The spiral structure of our Milky Way Galaxy". In: 499.2, pp. 473–482. DOI: 10.1051/0004-6361/200809692. arXiv: 0903.0721 [astro-ph.GA].
Hyman, S. D. et al. (2005). "A previously unknown radio transient source near the Galactic Centre". In: *Nature* 434, pp. 50–52. DOI: 10.1038/nature03400.
Intema, H. T. et al. (2009). "Ionospheric calibration of low-frequency radio interferometric observations". In: *A&A* 501, pp. 1185–1205. DOI: 10.1051/0004-6361/200811094.

Joye, W. A. and E. Mandel (Jan. 2003). "New Features of SAOImage DS9". In: *Astronomical Data Analysis Software and Systems XII*. Ed. by H. E. Payne, R. I. Jedrzejewski, and R. N. Hook. Vol. 295. Astronomical Society of the Pacific Conference Series, p. 489.

Lang, C. C., M. Morris, and L. Echevarria (1999). "Approaching the Epoch of Reionization with the Radio Arc". In: *ApJ* 526, pp. 727–743. DOI: 10.1086/308027.

Li, Z. et al. (1991). "The supernova rate in the Milky Way galaxy". In: *ApJ* 378, pp. 93–103. DOI: 10.1086/170413.

Mezger, P. G. and A. P. Henderson (1967). "Galactic H II Regions. I. Observations of Their Continuum Radiation at the Frequency 5 GHz". In: *The Astrophysical Journal* 147, p. 471. DOI: 10.1086/149030.

Morris, M. and E. Serabyn (1996). "The Galactic Center Environment". In: *ARA&A* 34, pp. 645–701. DOI: 10.1146/annurev.astro.34.1.645.

Navarro, Julio F., Carlos S. Frenk, and Simon D. M. White (May 1996). "The Structure of Cold Dark Matter Halos". In: 462, p. 563. DOI: 10.1086/177173. arXiv: astro-ph/9508025 [astro-ph].

Offringa, A. R. et al. (2014). "WSClean: an implementation of a fast, generic wide-field imager for radio astronomy". In: *MNRAS* 444, pp. 606–619. DOI: 10.1093/mnras/stu1368.

Offringa, A. R. and O. Smirnov (2017). "An optimized algorithm for multiscale wideband deconvolution of radio astronomical images". In: *MNRAS* 471, pp. 301–316. DOI: 10.1093/mnras/stx1368.

Perley, R. A. and B. J. Butler (2013). "An Accurate Flux Density Scale from 1 to 50 GHz". In: *ApJS* 204, p. 19. DOI: 10.1088/0067-0049/204/2/19.

Ranasinghe, S. and D. Leahy (2023). "A Statistical Analysis of Galactic Radio Supernova Remnants". In: *ApJS* 265, p. 53. DOI: 10.3847/1538-4365/acc1de.

Reynolds, S. P. (2008). "Supernova Remnants at High Energy". In: *ARA&A* 46, pp. 89–126. DOI: 10.1146/annurev.astro.46.060407.145237.

Roy, Subhashis and A. Pramesh Rao (Apr. 2004). "Sgr A* at low radio frequencies: Giant Metrewave Radio Telescope observations". In: 349.2, pp. L25–L29. DOI: 10.1111/j.1365-2966.2004.07693.x. arXiv: astro-ph/0402052 [astro-ph].

Roy, Subhashis and A. Pramesh Rao (2002a). "GMRT observations of four suspected supernova remnants near the Galactic Centre". In: *Monthly Notices of the Royal Astronomical Society* 329, pp. 775–786. DOI: 10.1046/j.1365-8711.2002.05007.x.

— (Feb. 2002b). "GMRT observations of four suspected supernova remnants near the Galactic Centre". In: 329.4, pp. 775–786. DOI: 10.1046/j.1365-8711.2002.05007.x. arXiv: astro-ph/0110104 [astro-ph].

Rybicki, G. B. and A. P. Lightman (1979). *Radiative Processes in Astrophysics*. Wiley-Interscience.

Sedov, L. I. (1959). *Similarity and Dimensional Methods in Mechanics*. Academic Press.

Shen, Juntai and Xing-Wu Zheng (Oct. 2020). "The bar and spiral arms in the Milky Way: structure and kinematics". In: *Research in Astronomy and Astrophysics* 20.10, 159, p. 159. DOI: 10.1088/1674-4527/20/10/159. arXiv: 2012.10130 [astro-ph.GA].

Strömgren, B. (1939). "The Physical State of Interstellar Hydrogen". In: *The Astrophysical Journal* 89, pp. 526–547. DOI: 10.1086/144074.

Su, Meng, Tracy R. Slatyer, and Douglas P. Finkbeiner (Dec. 2010). "Giant Gamma-ray Bubbles from Fermi-LAT: Active Galactic Nucleus Activity or Bipolar Galactic Wind?" In: 724.2, pp. 1044–1082. DOI: 10.1088/0004-637X/724/2/1044. arXiv: 1005.5480 [astro-ph.HE].

The CASA Team et al. (2022). "CASA, the Common Astronomy Software Applications for Radio Astronomy". In: *PASP* 134, p. 114501. DOI: 10.1088/1538-3873/ac9642.

Thompson, A. R., J. M. Moran, and G. W. Swenson Jr. (2017). *Interferometry and Synthesis in Radio Astronomy*. 3rd. Springer. DOI: 10.1007/978-3-319-44431-4.

Tingay, S. J., R. Goeke, J. D. Bowman, et al. (2013). "The Murchison Widefield Array: The Square Kilometre Array Precursor at Low Radio Frequencies". In: *PASA* 30, e007. DOI: 10.1017/pasa.2012.007.

Truelove, J. K. and C. F. McKee (1999). "Evolution of Nonradiative Supernova Remnants". In: *ApJS* 120, pp. 299–326. DOI: 10.1086/313176.

Wilson, T. L., K. Rohlfs, and S. Hüttemeister (2013). *Tools of Radio Astronomy*. 6th. Springer.

Woosley, S. E., A. Heger, and T. A. Weaver (2002). "The evolution and explosion of massive stars". In: *Rev. Mod. Phys.* 74, pp. 1015–1071. DOI: 10.1103/RevModPhys.74.1015.

Yusef-Zadeh, F. et al. (2022). "Statistical Properties of the Population of the Galactic Center Filaments: The Spectral Index and Equipartition Magnetic Field". In: *ApJL* 925, p. L18. DOI: 10.3847/2041-8213/ac4802.

Yusef-Zadeh, F., J. W. Hewitt, and W. Cotton (2004). "A 20 Centimeter Survey of the Galactic Center Region. I. Detection of Numerous Linear Filaments". In: *The Astrophysical Journal Supplement Series* 155.2, pp. 421–550. DOI: 10.1086/425338.

Yusef-Zadeh, F., M. Morris, and D. Chance (1984). "Large, highly organized radio structures near the galactic centre". In: *Nature* 310, pp. 557–561. DOI: 10.1038/310557a0.